A 17,000 yr paleomagnetic secular variation record from the southeast Alaskan margin: Regional and global correlations

M.H. Walczak[1,3], J.S. Stoner[1], A.C. Mix[1], J. Jaeger[2], G.P. Rosen[2], J.E.T. Channell[2], D. Heslop[3], C. Xuan[1,4]

1 – College of Earth, Ocean, and Atmospheric Sciences, Oregon State University, Corvallis OR 97331

2 – Department of Geological Sciences, University of Florida, Gainesville, FL 32611

3 – Research School of Earth Sciences, Australian National University, Canberra, ACT, 2612

4 – National Oceanography Centre Southampton, University of Southampton,

Abstract

High-resolution sedimentary records from two cores from the Gulf of Alaska margin allow development of a ~17,400 year reconstruction of paleomagnetic secular variation informing on regional and global variability. General agreement between the two records on their independent chronologies confirms that local PSV is recorded, demonstrating that such archives, notwithstanding complexities due to variable sedimentary regimes, deposition rates, and diagenetic conditions, can provide meaningful information on the past changes of the geomagnetic field. Comparisons with other independently-dated sedimentary paleomagnetic records from the greater Northeast Pacific indicate largely coherent inclination records that can be used to produce a regional inclination anomaly stack (NEPSIAS) capturing the common signal over an area spanning >30° longitude and latitude from Alaska through Oregon to Hawaii. Comparison of NEPSIAS with high quality declination records from the northern North Atlantic show significant similarity. Negative (shallow) anomalies in NEPSIAS inclination are associated with eastward NNA declination while positive (steep) anomalies in NEPSIAS inclination are associated with NNA westward declinations. The directional records can be compared to regional geomagnetic intensity over the past ~3000 years in North America and back nearly 9000 years in the Euro/Mediterranean region, suggesting oscillations in the relative strength of the North American flux lobe and Euro/Mediterranean extension of the Siberian flux lobe. This implicates a long-lived organizing structure imposed on the geomagnetic field, perhaps controlled by lower mantle and/or inner core heterogeneities, and supports the potential for stratigraphic correlation of directional PSV as a dating tool throughout the Holocene and perhaps beyond.

Comparisons of well-dated paleomagnetic secular variation (PSV) records from the Gulf of Alaska with other independently-dated records (Lake Waiau in Hawaii, Grandfather

Lake in Alaska, Fish Lake in Oregon) support the development of a well-defined stack extending back >15,000 cal ybp. This stack illustrates reproducible regional PSV and expands observations of regionally coherent Holocene geomagnetic behavior from Western North America into the Northeastern Pacific region. Covariance of steep inclination in the North Pacific with increased paleointensity in North America, reduced paleointensity in Europe, and westward shifts in declination in the North Atlantic region are consistent with a hypothesis that large scale PSV is driven by variability in the strength of relatively fixed regions of concentrated geomagnetic flux observed over Canada and Northern Eurasia in the modern and historic geomagnetic field. The relationship between Northeast Pacific inclination and North Atlantic declination appears to be consistent back ~12,000 cal ybp; this may indicate the Northern Hemisphere magnetic flux lobes are persistent on millennial scales, with implications for drivers of field morphology as well as the potential of PSV as a stratigraphic tool in the Holocene. Coherence in the inclination behavior of North Pacific records and declination behavior of European records over the Holocene does not support drift of the geomagnetic field as the predominant driver of PSV variability at mid-latitudes on millennial timescales. However, variability in the relative strength of spatially persistent flux lobe patches is a likely driver of 'dipole wobble'.

1. Introduction

1.1 Paleomagnetic secular variation

Averaged over tens of thousands of years, the earth's magnetic field can be approximated by a geocentric axial dipole (GAD) (Merrill, et al., 1996). However, at any

given moment the geomagnetic field expressed at the Earth's surface deviates substantially from this idealized morphology (Jackson et al., 2000). Field morphology changes with time, displaying variable tilt of the best-fitting dipole relative to the axis of rotation (Amit and Olson, 2008), as well as non-dipole structures (Merrill, et al., 1996). Our incomplete understanding of what drives deviation from a GAD, in conjunction with the unresolved temporal and spatial scales over which non-dipolar structures persist (Bloxham and Gubbins, 1987) precludes accurate prediction of future geomagnetic field behavior and hinders our ability to reconstruct past field morphologies. Historical reconstructions indicate the existence of persistent concentrations of geomagnetic flux, such as the Canadian and Siberian flux lobes (Bloxham and Gubbins, 1985), which may result from organizing structure imposed on the geomagnetic field by lower mantle heterogeneity (Bloxham and Gubbins, 1987; Bloxham, 2002; Gubbins et al., 2007). If so, patterns of paleomagnetic secular variation (PSV) are unlikely to be random, and the interplay of dipolar and non-dipolar components of the field may allow us to one day understand the dynamics of geomagnetic change.

Data-based reconstructions of the global geomagnetic field (e.g., Korte and Holme, 2010; Korte et al., 2011; Nilsson et al., 2010; 2011; 2014), as well as dynamo modeling studies (Bloxham, 2002; Gubbins et al., 2007; Davies et al., 2008; Amit et al., 2011) suggest that oscillations of flux concentrations at a few recurrent locations could be potential drivers of mid-latitude PSV. However alternative conceptual drivers of centennial-to millennial-scale PSV variability, including drift of non-dipole field sources (Thompson, 1984) or dipole wobble (Cox, 1962), remain plausible (Nilsson et al., 2010; 2014). Beyond the last 5000 years, high-quality observations of PSV behavior are

concentrated in the Atlantic sector of the northern hemisphere (Korte et al., 2011; Stoner et al., 2013), while those from the Pacific sector (e.g. Verosub et al., 1986; Peng and King, 1992; Geiss and Banerjee, 2003; Lisé-Pronovost et al., 2009) remain rare and with limited temporal resolution and/or chronological control. More detailed records, extending further back in time and covering a larger geographic range, are needed to facilitate a better understanding of the spatial dynamics of the geomagnetic field.

Continental margin sediments can provide greatly expanded, and in many cases well-dated, paleomagnetic records from widely distributed locations (e.g., Stoner and St-Onge, 2007). However, interpretations of paleomagnetic records from continental margin environments are potentially complicated by variable sedimentation rates, lithogenic sources, transport mechanics, and diagenetic conditions. We explore the development of PSV from the continental margin of the Gulf of Alaska using jumbo piston, trigger, and multi-cores collected during R/V Ewing cruise EW0408 in 2004 (Figure 1). Independent marine radiocarbon chronologies and lithologic variability assessed through computerized tomographic (CT) scans support the development of continuous high resolution PSV records that span ~6,200 years BP on an open continental shelf (site EW0408-79JC; 59.53° N, 141.76° W, 158 m depth) and ~17,000 years BP from a small depositional basin on the adjacent Kayak slope (site EW0408-85JC; 59.56° N, 144.15° W, 682 m depth). Comparisons with available independently-dated records from Alaska, Hawaii, Oregon, and the Western US allow us to evaluate the coherency of PSV throughout the Northeast Pacific as well as the relationship of Northeast Pacific PSV to records from the North Atlantic, Europe, and global field reconstructions.

1.2 Geologic setting: The Gulf of Alaska

The Gulf of Alaska is a tectonically active, glaciated margin. The mean shelf depth is ~140 m and is <40 km wide in the study area, with a shelf break depth of ~220 m. Sedimentation is overwhelmingly terrigenous, with major sources including the drainages of the Bering and Malaspina Glaciers, as well as the Copper River (Figure 1). Together, these distribution systems form the greatest source of terrigenous material (>200×10^6 tons yr^{-1}) to the Pacific Ocean from either American continent (Jaeger et al., 1998; Jaeger and Nittrouer, 2006), with modern accumulation rates on the shelf of ~0.1 – 3 cm/yr (Jaeger and Nittrouer, 2006). Thus the expanded lithogenic depositional sequences of the Alaskan shelf potentially allow for PSV reconstructions at a resolution impossible to capture in slowly-accumulating deep-ocean environments.

Although there is significant opportunity to record the geomagnetic field at high-resolution, marine continental margin records are prone to a variety of complications. The Gulf of Alaska shelf and slope are variable and energetic depositional environments, exposed to rapid near-bed current velocities associated with geostrophic acceleration of shelf-trapped coastal currents, wind-driven downwelling, and tides, as well as large winter storm events associated with the Aleutian Low (Weingartner et al., 2002). The sediment supply to the region is also diverse, associated with both the proximal erosion of the St. Elias Range Bering and Malaspina glaciers, as well as distal delivery from the catchment basin of the Copper River; these source lithologies differ in both magnetic mineralogy and grain-size (Cowen et al., 2006), potentially complicating interpretations of normalized remanence.

Waters above the shelf and slope are highly productive (Sambrotto and Lorenzen,

1987) and degradation of organic matter at and above the sea floor may drive sedimentary diagenesis. While benthic oxygen levels on the margin have been increasing through the Holocene, the early Holocene and late deglacial intervals experienced episodes of benthic hypoxia (Davies et al., 2011; Addison et al., 2012). This could allow for non-steady state degradation of paleomagnetic records via microbial destruction of primary iron-bearing magnetic remanence carriers during bacterially-mediated anaerobic sulphate reduction (Karlin and Levi, 1983; Tarduno and Wilkinson, 1996), and/or production of secondary magnetic minerals (Tarduno et al., 1998; Roberts et al., 2012).

2 Methods

2.1 Bulk Sediment Properties

Magnetic susceptibility and gamma-ray attenuation (GRA) bulk-density data were measured shipboard on whole cores on a GEOTEK MSCL-S multi-sensor track at 1 cm intervals. Point-source magnetic susceptibility was measured at 0.5 cm intervals in the multi-core, trigger-core, and uppermost sections of jumbo piston cores EW0408-85JC using a Bartington MS2E core logging sensor (Figure A.1).

2.2 Computerized tomographic (CT) scanning

Computerized tomographic (CT) density measurements were performed at the Oregon State University College of Veterinary Medicine using a Toshiba Aquilion 64 Slice instrument. Scans were collected at 120 kVp and 200 mAs. For visualization purposes, the resulting images were processed with a “sharp” algorithm to generate

perpendicular sagittal and coronal images every 4mm across the core. Down-core and across core pixel resolution within each slice is 500 μm. The cores were scanned in ~60 cm segments and then joined into a composite image using Adobe Photoshop software (Figure 2; Davies et al., 2011).

2.3 Radiocarbon Dating

Planktonic foraminifera were picked from the >150 μm sediment fraction. The two predominant planktonic species for the sites, *N. pachyderma* (sinistral) and *G. bulloides*, were analyzed separately at 604 centimeters below sea floor (cmbsf) in core EW0408-79JC, and at 555 cmbsf in core EW0408-85JC. The resultant *N. pachyderma* radiocarbon age is 10 ± 50 years younger than that for the *G.bulloides* in core EW0408-79JC, and 65 ± 50 years greater than that for the *G. bulloides* in core EW0408-85JC (Davies et al., 2011). As these differences approximate the measurement uncertainty for the individual samples, for all other depths the species were combined to increase sample size and reduce analytical error.

Radiocarbon analyses were performed at the UC Irvine Keck AMS facility. A total of 38 radiocarbon measurements were performed for 37 stratigraphic horizons in core EW0408-85JC: 3 planktonic samples from the trigger core, and 35 planktonic samples from the jumbo piston core (Table A.1; Davies-Walczak et al., 2014). A total of 11 radiocarbon measurements were performed for 10 stratigraphic horizons in core EW0408-79JC (Table A.1). The raw radiocarbon dates were converted to a calendar age scale using the Marine13 curve in CALIB 7.0 (Stuiver and Reimer, 1993). To account for regional surface-water reservoir ages of 880 ± 80 years, a constant ΔR of 470 ± 80 years

was applied to all planktonic foraminiferal dates (Davies-Walczak et al., 2014). As the uppermost trigger core sample (22 cmbsf) in EW0408-85JC gives a raw radiocarbon age of 660 ± 250, implying a negative surface ocean reservoir age, we infer some degree of post-bomb contamination and exclude it from further analysis (Davies-Walczak et al., 2014). To generate age-depth relationships for the cores, we apply a Bayesian probabilistic model (BChron; Haslett and Parnell, 2008) to the remaining calibrated planktonic foraminiferal dates, assuming constant reservoir ages with respect to a changing atmosphere (Davies-Walczak et al., 2014).

2.4 Magnetic Methods

Natural remanent magnetization (NRM) of u-channel samples was measured using a 2G Enterprises cryogenic magnetometer at the Paleomagnetism and Environmental Magnetism Laboratory at University of Florida. NRM measurements were performed at 1-cm spacing, though each data point reflects an integral within the magnetometer's pickup coils detection window, which is equivalent to a Gaussian response function (~4.5 cm width at half height; Weeks et al., 1993). Measurements were made before demagnetization and after 14 alternating-field (AF) demagnetization steps with peak AF from 10-100 mT at 5 mT increments between 10-50 mT and 10 mT increments between 50-100 mT. Declination, inclination, and intensity data were processed using the Microsoft Excel routine Macro-Uch-1.xls (Mazaud, 2005), and component magnetic directions and their maximum angular deviation (MAD) were calculated using the principal component method (Kirschvink, 1980) using all steps from 10-60 mT to establish their characteristic remanent magnetization (ChRM).

Low-field volumetric magnetic susceptibility (κ) measurements of u-channel samples were performed at 1-cm spacing using a track built at the University of Florida using a Saffire Instruments SI2B magnetic susceptibility loop system with an approximately Gaussian response function of ~3 cm width at half-height (Thomas et al., 2003). Anhysteretic remanent magnetization (ARM), also expressed as a susceptibility of ARM (κ_{ARM}), was applied to each u-channel in a peak AF of 100 mT, with a 50 μT direct current (DC) bias field, and measured at 1-cm intervals prior to and after AF demagnetization at the same steps used for NRM up to 80 mT. Isothermal remanent magnetizations (IRM) were produced using pulsed DC fields of 0.3T ($IRM_{0.3T}$) and 0.95 T ($IRM_{0.95T}$, assumed to represent a saturating field and generate a saturation isothermal remanent magnetization or SIRM) applied down the +Z axis and a reversed DC field of 0.3 T applied down – Z axis ($IRM_{-0.3T}$). The $IRM_{0.3T}$ was measured prior to and after demagnetization at the same steps used for ARM, while the $IRM_{0.95T}$ and $IRM_{-0.3T}$ were measured prior to and after AF demagnetization at peak fields of 30 and 60 mT. To evaluate coercivity and magnetic mineralogy, S-ratios were calculated according to Bloemendal et al., (1992), via normalization of the $IRM_{-0.3T}$ by the $IRM_{0.95T}$ (again, assumed to reflect SIRM). Values approaching -1 indicate lower coercivity and ferromagnetic mineralogy (e.g. magnetite), while values closer to zero indicate higher coercivity and a potentially higher contribution of antiferromagnetic mineralogy (e.g. hematite).

To better evaluate potential variability of magnetic remanence carriers through the lithologic units of EW0408-85TC/JC, hysteresis, backfield, IRM thermal demagnetization, and room temperature to low-temperature SIRM (RTLTSIRM)

experiments were performed on nine samples from the late Holocene, early Holocene/deglacial transition, and late glacial portions of the core at the Institute for Rock Magnetism at the University of Minnesota. Hysteresis parameters including saturation remanence (M_{rs}), saturation magnetization (M_s), coercivity (H_c), and coercivity of remanence (H_{cr}) were acquired and IRM was imparted for thermal demagnetization measurements in a saturating field of 1000 mT on a Princeton Measurements Corporation MicroMag vibrating sample magnetometer (VSM). A 2.5T SIRM was acquired and measured while cooling from 300 K to 10 K and then warming back to 300K (RTLTSIRM) on a Quantum Design Magnetic Properties Measurement System. Additional hysteresis and backfield measurements for EW0408-85JC were made using a VSM at the Pacific NW Paleomagnetism Laboratory at Western Washington University.

3 Results

3.1 Generation of composite depth scale

Composite sediment depths in centimeters-below-sea-floor (cmbsf) were established empirically using visual correlation of point-source magnetic susceptibility and gamma density data to align the jumbo piston cores with their trigger cores and attendant multi-cores (Figure A.1). At the site of core EW0408-79JC, the jumbo piston core did not detectably lose sediment at the top of the core. Trigger core EW0408-79TC apparently lost 13 cm due to over-penetration, while multi-core EW0408-78MC7 captured the sediment/water interface. The resultant cmbsf scale for site EW0408-79JC therefore adds 13 cm to measured trigger core depths. At the site of core EW0408-85JC, the jumbo piston core lost 150 cm of core top. Trigger core EW0408-85TC lost 13 cm of

core top, while the multi-core EW0408-84MC8 successfully captured the sediment/water interface. Therefore, to generate a composite cmbsf scale for site EW0408-85JC, 150 cm were added to measured jumbo core depths and 13 cm were added to measured trigger core depths (Davies et al., 2011).

3.2 Chronology

Assuming constant accumulation rates below the deepest dated interval (1204 cmbsf), the portion of shelf core EW0408-79JC not disturbed by coring (0 to 1350 cmbsf) spans 6,260 cal ybp (Figure 3). Accumulation rates range from ~100 to 800 cm/kyr in the jumbo piston core, with highest sedimentation rates in the upper 600 cmbsf (~1,500 cal ybp), peaking in the 200 to 500 cmbsf interval (~800 to 1000 cal ybp) presumably associated with a neoglacial expansion of the South Alaskan glacial system (Wiles et al.,2008; Barclay et al., 2013). Slope core EW0408-85JC spans 17,400 cal ybp (Figure 3), and documents the most recent deglaciation of the Northeast Pacific (Davies et al., 2011). Accumulation rates range from ~10 cm/kyr during the laminated Bolling and post-Younger Dryas intervals of global deglaciation, to >500 cm/kyr during ice-proximal marine sedimentation in the lower 440 cm of the core.

3.3 Stratigraphy

The lithology of shelf core EW0408-79JC is a dark greenish-gray bioturbated silty clay, with interbedded sand/silt layers ranging from sub-millimeter to several centimeters in thickness throughout the core. The CT-scan imagery shows strong vertical deformation structures in the sediment below 1350 cmbsf (Figure 2b), reflecting sediment

drawn rapidly into the core barrel following the penetration of several cohesive, sandy layers. As this portion of the recovery reflects a complete distortion of primary depositional fabric, it has been excluded from interpretation.

The CT scan imagery, supported by MSCL data and radiocarbon dates, suggest core EW0408-79JC can be crudely divided into two distinct depositional units (Figure 2). The interval from 0 to 550 cmbsf display well-preserved (450 – 400 cmbsf) to partially-bioturbated laminations and bi-modal densities averaging ~1.79 ± 0.1 g/cm^3, contrasting with a more homogenous unit between ~550-1200 cmbsf characterized by overall higher density (~1.82 ± 0.04 g/cm^3) and punctuated by occasional sandy layers with sharp and sometimes erosive basal contacts. At depths ~1200-1350 cmbsf, CT scans suggest a similar lithofacies to the uppermost portion of the core, with strong density contrasts and the appearance of partially-bioturbated laminations (Figure 2). The preservation of laminations on the oxygenated shelf suggests that episodic (perhaps instantaneous) sedimentation rates exceed 2 cm/yr (Jaeger and Nittrouer, 2006) in those intervals.

The homogenous sandier unit between ~550-1200 cmbsf is capped at 575-705 cmbsf by a massive sandy-silt layer with anomalously high κ and a sharp basal contact (Figures 2 and 4). This massive unit has a magnetic and bulk lithology distinct from the overlying and underlying sediments and may have been deposited instantaneously. As a result we exclude these depths from paleomagnetic interpretation (Figure 4).

Slope core EW0408-85JC captures distinct changes in lithology that reflect the environmental history of the Gulf of Alaska over the last 17,400 years, including the retreat of the Cordilleran ice sheet in the late Pleistocene and large-scale oceanographic changes during the transition into relatively stable Holocene climate conditions (Figure 2)

(Davies et al., 2011). The deepest unit, from the base of the core at ~1270 cmbsf to 831 cmbsf, consists of a massive dark gray diamict interpreted as reflecting ice-proximal glacial-marine sedimentation (Davies et al., 2011). At 831 cmbsf there is a sharp contact with a relatively low-density laminated unit 34 cm thick (Figure 2d), reflecting high primary productivity and low bottom-water oxygen content, an interpretation supported by excess concentrations of Mo and U (Davies et al., 2011; Addison et al., 2012). There is an increase in lithogenic sediment with coarse pebbles interpreted as ice-rafted debris between 797 and 745 cmbsf (Figure 2b). This unit reflects a return to glacial conditions accompanying a decrease in primary productivity and renewed bottom-water oxygen (Davies et al., 2011; Addison et al., 2012). From 745-0 cmbsf, sedimentation at the site is broadly characterized by bioturbated dark-gray silty clays, although the interval from 730-745 cmbsf is weakly laminated and has elevated Mo and U contents, indicating a second episode of low bottom-water oxygen in the early Holocene (Davies et al., 2011; Addison et al., 2012).

3.4 Natural and Laboratory Remanent Magnetizations

Figures 4 and 5 show the NRM intensities, ChRM directions and their associated MAD values, magnetic susceptibility, ARM and IRM intensities, S-ratios, κ_{ARM}/κ, and sedimentation rates for jumbo piston cores EW0408-79JC and EW0408-85JC (Figures A.2 and A.3 present the same data for the associated multi- and trigger cores). Due to lack of azimuthal orientation, declinations are initially rotated to a core mean of zero. ChRM inclinations from both cores are close to their GAD expected values (~ 74°) suggesting that the geomagnetic field is being recorded with directional fidelity.

For EW0408-79JC, MAD values are generally less than 2° throughout the core, indicating consistently well-defined magnetizations. However, centimeter-scale variations in directions, intensity, and MAD values occur in sediments with partially- to well-preserved primary depositional structures from 0-500 cmbsf (<1,100 cal ybp) and at depths greater than 1200 cmbsf (>5,500 cal ybp), suggesting that this 'noise' results from fine scale sedimentological heterogeneity. NRM, ARM and IRM intensities (after 30 mT AF demagnetization) are consistently high (0.041 ± 0.013 A/m, 0.023 ± 0.004 A/m, and 1.61 ± 0.22 A/m, respectively) with minimal down-core trends, although increases in NRM, ARM, and IRM intensities are observed in the lower-sedimentation rate/higher-density depositional unit between 550 - 1200 cmbsf (Figure 4). S-ratios vary around 0.95 and κ_{ARM}/κ values vary around 1.4, implying a relatively consistent ferrimagnetic mineralogy of generally uniform average magnetic grain-size, estimated to be ~ 5 μm using the calibration of King et al., (1982).

Core EW0408-85JC, in contrast to the shelf site, exhibits pronounced millennial-scale changes in magnetic properties, reflecting the evolution of the depositional environment over the last 17,400 years (Figure 5). NRM, ARM and IRM (after 30 mT AF demagnetization) have respective means of 0.018 ± 0.016 A/m, 0.015 ± 0.01 A/m and 0.95 ± 0.5 A/m (Figure 5), showing greater variance, albeit over a much longer time interval, than observed at EW0408-79JC. Low remanence concentrations observed between ~ 550-840 cmbsf contrast with higher intensities at the top and bottom of the core, driving the much greater long-term variability. The S-ratio and κ_{ARM}/κ follow a similar pattern, with lower values in the central part of the core, consistent with magnetic mineralogy and/or grain-size changes.

High magnetic intensities in EW0408-85JC are observed between the core top and 530 cmbsf (<7,200 cal ybp) and below 800 cmbsf (>13,500 cal ybp). MAD values follow suit, with the upper ~ 530 cmbsf displaying well-defined magnetization with values mostly < 1°. MAD values are more variable below 530 cmbsf, though generally less than 10° except for the deglacial interval between 715-795 cmbsf (~10,100-12,700 cal ybp) that is characterized by much lower NRM intensities ($8 \times 10^{-4} \pm 6 \times 10^{-4}$ A/m at 30 mT AF demagnetization), MAD values approaching 40°, and component inclinations varying around a mean ~15° shallower than the GAD prediction for the site latitude.

Because the most poorly resolved directions in EW0408-85JC are found in the part of the core with the lowest intensities, and hence are sensitive to measurement noise as lower coercivity and more magnetic phases become increasingly demagnetized, component directions were also calculated using the 7 most consistent directions from the 14 AF demagnetization steps from 10-100 mT (Figures A.4 and 5). For most of the record these optimized components result in essentially identical directions to those determined using all steps, though with (by definition) improved MAD values (Figures A.4 and 5). The only significant differences occur in the lowest intensity interval, ~710-850 cmbsf, 10 to 13 kybp, where MAD values are significantly reduced from as high as around 40° to <10° and the resultant directions show reduced variability and improved serial correlation with overall steeper and more GAD-like inclinations (Figure A.4). The optimized ChRM directions are similar to those obtained from the 20 mT AF demagnetization step, suggesting that the optimized component directions largely reflect a low-coercivity primary magnetization appropriate for recording PSV.

3.5 Temperature dependent and infield magnetic measurements

Examination of magnetic hysteresis properties, thermal demagnetization behavior (Ms/T), and low-temperature remanence (RTLTSIRM) curves allows further insights into the magnetic properties of EW0408-85JC (Figure 6; Figure A.5). Outside of the low intensity interval in 85JC (~710-850 cmbsf), ratios derived from the hysteresis parameters plot in the pseudo single domain (PSD) field of a Day et al., (1977) diagram (Figure 6a), falling slightly above the theoretical magnetite SD to MD mixing line (Dunlop, 2002). In the low intensity interval, in contrast, hysteresis ratios are much more scattered with coercivity ratios much higher (Figure 6a) than would be expected for the magnetite (e.g. Dunlop, 2002). Low S-ratios (<0.9) are also observed in this interval providing additional evidence for a greater proportion of high coercivity magnetic minerals (Figure 5).

A more detailed examination of the rock magnetic properties was performed on nine samples spanning the range of sediment lithologies present in EW0408-85TC/JC: three from Holocene sediments (62, 399, and 649 cmbsf), two from the organic-rich material deposited during deglaciation (777.5 and 808 cmbsf), and four from the late glacial diamict (850, 859, 949, and 1199 cmbsf). All hysteresis loops (detrended to correct for the slope of the paramagnetic contribution) are broadly consistent with a magnetite mineralogy (Figure A.5), although hysteresis loop widths from samples 777.5, 808, and 850 cmbsf are somewhat greater than for samples above (62 and 399 cmbsf) and below (859-1199 cmbsf), suggestive of a high-coercivity contribution to remanence (e.g., hematite; Tauxe 1998). The thermal demagnetization curves from all depths measured show a Curie point of ~580 C, indicative of magnetite (Figure 6c). A transient increase in

magnetization starting at ~400 C may indicate some contribution from Ti-poor titanomagnetite or titanium maghemite exolving to form magnetite (Ozdemir and O'Reilly, 1981). The role of magnetite as a remanence carrier is supported by the RTLTSIRM curves, all of which display a transition at ~120 K (e.g., Verwey, 1939) (Figure 6d) that is considered to be diagnostic of magnetite (e.g., Jackson et al., 2011). However, samples between 649 and 808 cmbsf (less 777.5 cmbsf, for which no data is available) have a weaker transition and a 'humped' appearance between 300 K and the ~120 K 'Verwey' transition, likely related to the convolved presence of maghemite and magnetite (Ozdemir and Dunlop, 2010). The presence of a high-coercivity remanence carrier in this interval is further supported by the backfield curves (Figure 6b) and high Hcr values (Figure A.6). These higher Hcr values observed for the deglacial (~710-850 cmbsf) interval persist in the post-heating Hcr curves, supporting an interpretation of hematite or maghemite over other high-coercivity minerals such as goethite that have much lower curie temperatures (e.g., Ozdemir and Dunlop, 1996).

4. Discussion

4.1 Magnetic remanence carriers and geomagnetic recording fidelity

Although the preservation of physical structure in EW0408-79JC argues that sedimentation is episodic on short, perhaps annual, timescales (e.g., Jaeger and Nittrouer, 2006), the overall high deposition rate and general sedmentary consistency implies that PSV features on centennial to millennial timescales should be preserved with little if any smoothing or temporal offset. With the exception of the massive sandy-silt interval excluded from interpretation (Figure 4), ARM and IRM magnetizations, S-ratios and

κ_{ARM}/κ values in EW0408-79JC all suggest the presence of a homogeneous population of low-coercivity magnetic remanence carriers (i.e. magnetite) through most of the last 6,200 years.

The longer record in core EW0408-85JC displays a more complicated depositional and preservation history. A low-intensity interval between ~530-800 cmbsf (~7,200-13,500 cal ybp; Figure 5), indicates a change in magnetic mineralogy likely driven by the combined effects of changing sediment source, transport, and depositional regime along with early diagenesis (e.g. Karlin and Levi, 1983), the latter perhaps related to the well-known discrete episodes of deglacial benthic hypoxia (e.g., Barron et al., 2009; Davies et al., 2011; Addison et al., 2012). S-ratios below 0.9 (Figure 5) and elevated H_{cr} (Figures A.5 and A.6) document a magnetic assemblage with a greater proportion of high-coercivity minerals (e.g. hematite, maghemite) over the 710-850 cmbsf interval. However, the presence of magnetite is clearly indicated by Curie temperature analyses, Verwey transitions (Figure 6), as well as by hysteresis data (Figure A.5), through the deglacial and early Holocene portions of the core. We thus infer that a primary (depositional or post-depositional) remanent magnetization is preserved with directions that can be interpreted as geomagnetic in origin throughout the EW0408-85JC record, though with less precision during the diagenetically-affected interval between 710 – 850 cm / 10,000 – 14,700 cal ybp. Lithologic variability in excess of recommended criteria (Tauxe, 1993) make both EW0408-85JC and EW0408-79JC non-ideal candidates for relative paleointensity reconstructions.

4.2 Paleomagnetic secular variation

Figure 7 shows the composite (trigger core/jumbo piston core) ChRM directions for the EW0408 sites on their independent age models compared with global field model predictions for the site location. Inclinations at both sites, smoothed using a Gaussian filter with a 100-year 1σ width to facilitate comparison, are generally consistent with historical (GUFM1; Jackson et al., 2000) and paleo (CALS7K.2; Korte and Constable, 2005; CALS10K.1b; Korte et al., 2011; FBNKE; Nilsson et al., 2010) global field model predictions. Similarities over the last 3000 cal ybp, particularly between EW0408-85TC/JC and the more detailed CALS7K.2 model, suggest that PSV is recorded by these continental margin sediments and, in turn, that the model captures field dynamics in a region poorly constrained by prior data. Distinctions do exist; for example the almost 20° change from low to high inclination at ~ 950 cal ybp in EW0408-79JC is much greater than global field models predict. Unfortunately, part of this inclination event occurs within a core break at EW0408-85TC (Figure A.3) and is thus not as well recovered, but it is consistent with a similar inclination event recorded in volcanic (Hagstrum and Champion, 2002) and archeomagnetic data (Hagstrum and Blinman 2010) from the western US. In general the CALS10K.1b model predicts less variability than observed in either record, although there is considerable similarity on millennial timescales (Figure 7).

The older part of the EW0408-85JC PSV record (>10,000 cal ybp) suggests larger amplitude millennial-scale variability than is observed in the Holocene, though it is conceivable that part of this variability could result from uncorrected diagenetic influence on the PSV record (between ~10,000-14,700 cal ybp, as discussed in section 4.1) and should be initially treated as suspect. Global field models provide no assistance during

this time interval, however, the independently dated (via 8 radiocarbon dates) Grandfather Lake, Alaska PSV record (Geiss and Banerjee, 2003) only 700 km WNW of the EW0408-85JC site also preserves high amplitude inclination variations prior to 10,000 cal ybp (Figure 8).

As with any sedimentary PSV record obtained via piston coring, declinations are somewhat less straightforward than inclinations. Several additional corrections were made after initially rotating the mean declination of each core to zero. The most significant was removal of linear trend from EW0408-85TC, consistent with rotation during core penetration. The linear-corrected declination was then rotated to be consistent with historical GUFM model predictions (mean declination for the last 400 yrs is ~ 28°) to correct for the lack of azimuthal control (Figure 7). EW0408-85JC declinations were then rotated to match the mean of the trigger core. Section 2 was rotated an additional 20° to account for misalignment during core splitting clearly visible on the core liner. The resulting declination time series from EW0408-85TC/JC and EW0408-79JC are similar and appear to agree with the global paleo field models for the last 4000 yrs (Figure 7). Both EW0408-85TC/JC and EW0408-79JC declinations similarly deviate from CALS10K.1b predictions in the 4-7 kyr interval, while showing more agreement below (Figure 7).

More independently-dated regional records will be required before these Gulf of Alaska PSV records can be fully validated. With that caveat, the chronologies of both cores are robust, and the paleomagnetic directional record is well preserved through most of both cores. The similarity of these records over their period of overlap when evaluated on their independent age models, as well as their similarity with global field model

predictions, further supports the notion that these continental margin sediments preserve centennial to millennial-scale geomagnetic field history for the south Alaska region.

4.3 Regional PSV comparisons and generation of a NE Pacific stack

Negative inclination anomalies of much greater magnitudes than have been observed historically, characterized by gradual growth and abrupt recovery transitions, have been recognized in volcanic (Hagstrum and Champion, 2002) and archeomagnetic (Hagstrum and Blinman, 2010) PSV records from the western US. Similar features have been found in sediment PSV records from the central (Lund and Banerjee, 1985; Lund, 1996) and western US (Verosub et al., 1986). Building upon historical (Barraclough and Thompson, 1982) and paleomagnetic (Lund, 1996) observations, the apparent similarity of PSV in the western US (Verosub et al., 1986; Hagstrum and Champion, 2002; Hagstrum and Blinman, 2010) with sites in Alaska (Geiss and Banerjee, 2002), the Chukchi Sea (Lisé-Pronovost et al., 2009) and the Beaufort Sea (Barletta et al., 2010) implies that at least some aspects of the geomagnetic field behave coherently over roughly a continental scale (e.g., Lund 1996). However the lack of strong independent chronologies for many of these records has remained the weakest point of this hypothesis.

Stacking independently-dated regional records from different depositional environments helps to circumvent errors which accompany the recording, preservation, and recovery process at individual sites by enhancing elements that covary between sites, and minimizing local variations that are not seen in multiple sites. Any resulting coherence is likely to reflect regional geomagnetic history, with a quantifiable estimate of uncertainty. In addition to the EW0408-85TC/JC PSV record we include three

continuous, independently-dated Pacific-sector paleomagnetic records of Holocene PSV in a stack: Lake Waiau, Hawaii Core 82-2 (19.8° N, 155.5° W; Peng and King, 1992), Fish Lake, Oregon (42.7° N, 118.7°W; Verosub al., 1986), and Grandfather Lake, Alaska (59.8°, 158.6° W; Geiss and Banerjee, 2003). While we note EW0408-79JC and EW0408-85JC show consistent PSV behavior for their period of overlap, we elect to use only EW0408-85TC/JC in the generation of this Northeast Pacific Stack as this record is of similar resolution to the others and our focus is on longer-term variability and spatial coherence. Lake Waiau core 82-2 is evaluated on an updated age model using the published dates recalibrated to Intcal13 via CALIB 7.0 (Peng and King, 1992; Stuiver and Reimer, 1993). Fish Lake, Oregon (42.7° N, 118.7°W; Verosub al., 1986), is presented on the adjusted chronology proposed by Hagstrum and Champion (2002) for the upper part of the record with an updated radiocarbon calibration to Intcal13, avoiding the mixed use of radiocarbon and tephra ages (e.g., Verosub et al., 1986) that complicates the application of modern calibrations in the early Holocene.

In order to evaluate the coherence of Holocene geomagnetic inclination records across 30° in latitude, we subtract the GAD-predicted inclination for each site location from the inclination record, noting that in the case of Fish Lake, an inclination correction of ~5° has already been applied (Verosub et al., 1986). The resulting records of inclination deviation from GAD (ΔI) were then interpolated to a constant resolution of 100 years on their independent chronologies through intervals for which data was collected, and an average ΔI value was calculated across all cores available for each time point (Figure 8).

The North Pacific PSV declination stack was generated in much the same way as

the inclination stack: available records were rotated to a mean of 0, filtered with a Gaussian filter of 100-year 1-σ width and interpolated to a constant 100-year resolution on their independent chronologies, and averaged at each time step across all cores for which data was available (Figure A.7). Grandfather Lake, however, provides no declination data due to lack of azimuthal orientation of the 1-m Livingston core drives during core collection (Geiss and Banerjee, 2003). As a result our declination stack includes only three regional North Pacific records, therefore our primary focus will be on the inclination record.

Although the age models are of varying resolutions and accuracies, and the depositional environments are diverse and widely dispersed, a number of robustly defined, millennial-scale inclination anomalies (ΔI), both positive and negative, appear as coherent features captured in the NE Pacific sedimentary inclination anomaly stack (NEPSIAS). The three largest -ΔI anomalies are found in the late Holocene: two well-known -ΔI events from regional records at ~1,400, and ~3,000 (e.g., Hagstrum and Champion, 2002; Herrero-Bervera and Valet, 2007; Hagstrum and Blinman, 2010), and a third at ~ 4,000 cal ybp. The latter is observed in stacks created using CALS7k.2 model predictions from the same locations, while more recent models only capture the younger two (Figure 8). Considering NRM acquisition and stacking-induced smoothing, the amplitude and rates of change of these ΔI features within NEPSIAS are likely minimum estimates, although they are somewhat larger than suggested by global field models, even when corrected for inclination shallowing by scaling the means to those predicted by the field models. Additional -ΔI anomalies are observed in the early to mid-Holocene, centered at ~6,500 and ~8,000 cal ybp, both of which are captured by CALS10k although

in this case model predictions suggests a larger -ΔI anomaly. The stacked records also extend beyond the limit of global field models, capturing an additional broad -ΔI anomaly centered around 11,000 cal ybp, with EW0408-85JC suggesting another large -ΔI anomaly at ~ 15,000 cal ybp. (Figure 8).

4.4 Drivers of Northern Hemisphere paleomagnetic secular variation

Deviations from GAD similar to those in NEPSIAS have been observed at similar times in high-resolution North Atlantic PSV records (e.g., Stoner et al., 2013). In the northern North Atlantic (NNA) these deviations are primarily expressed as large eastward shifts in declination associated with highs in European/Mediterranean archeomagnetic intensity over the last ~ 9000 cal ybp (e.g., Genevey et al., 2008; Gallet et al., 2015). NEPSIAS builds upon these observations by showing that -ΔI anomalies in the Northeast Pacific are roughly synchronous with eastward NNA declinations over the full 11,500 year length of the NNA record (Stoner et al., 2013) (Figures 9 and 10).

Although the overall morphology of NEPSIAS and NNA declination records are similar, NEPSIAS -ΔI anomalies appear to slightly lead eastward changes in NNA declination. Comparison with archeomagnetic (Hagstrum and Blinman, 2010) and lava-based (Hagstrum and Champion, 2002) inclination reconstructions, however, show no detectable temporal offset with NNA declination (Figure 9). The apparent lead is therefore likely an artifact of NEPSIAS, possibly as a result of the sediment magnetization acquisition process or systematic dating uncertainties. Steeper NEPSIAS inclinations are associated with westward NNA declination shifts and, for the last ~ 3000 cal ybp, higher North American intensities (e.g., Genevey et al., 2008); although little

North American intensity data is available beyond 3000 cal ybp, the relationship between NEPSIAS inclination and NNA declination appears to hold through the last 11,500 cal ybp (Figures 9 and 10).

Well-resolved PSV reconstructions spanning the last 5,000 years indicate that field morphology can be roughly broken into two modes consistent with a geomagnetic flux lobe over North America alternating in dominance with a flux lobe over Europe (Gallet et al., 2009; Stoner et al., 2013). The 'North American mode', characterized by relatively steep inclinations and high intensities in N. America, westward declinations in the N. Atlantic, and low intensities in Europe, is conceptually consistent with the time-averaged historical field of the past few centuries (Bloxham and Gubbins, 1985; Jackson et al., 2000). The alternate 'European mode' is characterized by periods of shallow inclination and low intensity in N. America, eastward declinations in the N. Atlantic, and high intensities in Europe, consistent with the time-averaged mid-to-late Holocene field (Korte and Constable, 2005; Amit et al., 2011). Inflection points for either steep NEPSIAS inclinations and westward NNA declinations, or shallow NEPSIAS inclination and eastward NNA declination, coincide with archeomagnetic jerks defined by Gallet et al., (2002) over the last ~3000 cal ybp (Figure 10). Based on this relationship, changes in NEPSIAS inclination may predict archeomagnetic jerks and/or periods of enhanced dipole eccentricity (Gallet et al., 2009) beyond the temporal limit of archeomagnetic data.

Observations of coherent inclination changes across a vast, though as yet poorly-defined, area in the Northeast Pacific are generally consistent with the idea of a regional 'dipole window' (Cox, 1962), and the concept of subdued secular variation in the Pacific has a long history. Secular variation in the Pacific nonetheless appears to co-vary with

that in the dynamic Atlantic, suggesting that the Pacific is sensitive to temporal variability in the relative strength of distal flux-lobe features in quasi-persistent locations under North America and Europe. Comparison of NE Pacific virtual geomagnetic poles (VGP) with global VGP reconstructions (Nilsson et al., 2011) and those from the NNA (Stoner et al., 2013) shed further light on these dynamics. Both VGP latitude and longitude show similarities in relative variability between the NE Pacific, NNA, and globally. Intervals of increased dipole tilt appear in synch with -ΔI in NEPSIAS, eastward NNA declination, and high Euro/Mediterranean intensity; all associated with the 'European Mode' of field behavior over the last 4,500 ybp (Figure 10). Earlier in the Holocene, between 4,500-8,000 cal ybp, the relationship shifts and increased dipole tilt is associated with +ΔI in NEPSIAS and westward declinations in the NNA; this is directionally consistent with the 'North American' mode of field behavior as defined for the late Holocene, although North American intensity is unfortunately poorly constrained beyond ~3,000 cal ybp (Figure 10). The transition from increased dipole tilt association with the 'North American mode' to the 'European mode' at ~4,500 cal ybp appears to be associated with the shift to overall higher global geomagnetic intensities in the late Holocene (Figure 10) and is consistent with the timing of a change in field morphology noted by Creer and Tucholka (1982).

The largest deviations from a geocentric axial dipole (GAD) in the Northern Hemisphere are observed during the highest reconstructed geomagnetic intensities of the Holocene, in contrast to the usual assumption that higher global intensity results in a more dipolar field (e.g., Merril et al., 1996). These observations are consistent with the idea that much of Holocene PSV and dipole eccentricity (Gallet et al., 2009) result from

temporal oscillations of high latitude flux concentrations at a few recurrent locations (Stoner et al., 2013). The existence of an ephemeral Euro/Mediterranean VGP attractor could also be an important component of PSV in the North Atlantic (Stoner et al., 2013), extended by NAPSIAS to the NE Pacific. The temporal and spatial scale of these observations strongly implicates a long-lived process, such as thermal heterogeneity of the lower mantle (Bloxham and Gubbins, 1987; Amit et al., 2011) or variability in the inner core (Aubert et al., 2013), imposing structure on the outer core that the geodynamo oscillates within.

5. Summary and Conclusions

High-resolution sedimentary records from two cores on the open continental shelf (EW0408-79JC) and slope (EW0408-85JC) of the Gulf of Alaska margin allow development of a ~17,400 year record of regional geomagnetic variability. General agreement between the two records on their independent chronologies confirms that local PSV is recorded, demonstrating that such archives, notwithstanding complexities due to variable sedimentary regimes, deposition rates, and diagenetic conditions, can provide meaningful information on the past changes of the geomagnetic field. Much, but not all, of the observed directional variability is consistent with spherical harmonic (CALS7K.2; Korte and Constable, 2011; CALS10K.1b; Korte et al., 2011) and/or VGP (FBNKE; Nilsson et al., 2010) predictions, suggesting that PSV in this location is likely governed by large scale geomagnetic dynamics as there was little prior regional data to constrain the models. Comparisons with other independently-dated sedimentary paleomagnetic records from the greater Northeast Pacific region (Verosub et al., 1986; Peng and King,

1992; Geiss and Banerjee, 2003) indicate largely coherent inclination records that can be used to produce a Northeast Pacific sedimentary inclination stack (NEPSIAS) capturing the common signal over a > 30° longitude and latitude region spanning from Alaska through Oregon to Hawaii (Figure 8).

Comparison of NEPSIAS with high quality declination records from the northern North Atlantic show significant similarity, and correlation could be further improved with slight age adjustments consistent with lock-in processes. NEPSIAS - ΔI anomalies are associated with eastward NNA declination and NEPSIAS + ΔI anomalies are associated with NNA westward declinations (Figures 9 and 10). The directional records can be compared to regional geomagnetic intensity, over the past ~3000 years in the North America and back nearly 9000 years in the Euro/Mediterranean region (e.g., Genevey et al., 2008; Gallet et al., 2015); these observations suggest oscillations between the 'North American' and 'European' modes of PSV organization that may be driven by variability in the relative strength of the North American flux lobe and Euro/Mediterranean extension of the Siberian flux lobe (Gallet et al., 2009; Stoner et al., 2013). If so, the persistence of these features implicates a long-lived organizing structure imposed on the geomagnetic field, perhaps by the lower mantle (Bloxham and Gubbins, 1987; Bloxham, 2002; Gubbins et al., 2007) and/or inner core heterogeneities (Aubert et al., 2013) that profoundly influences the spatial and temporal patterns of PSV. Additional continuous and independently-dated PSV records are required to assess the spatial and temporal scales over which these geomagnetic structures persist. Nonetheless, our growing understanding of the relationship between geomagnetic variability in the NE Pacific compared with the North Atlantic supports the potential for stratigraphic correlation of

directional PSV as a dating tool throughout the Holocene and perhaps beyond.

6 Acknowledgements

The authors gratefully acknowledge the crew and science party of R/V Maurice Ewing cruise EW0408, the staff of the OSU Marine Geology Repository, the OSU CEOAS Stable Isotope laboratory, the UC Irvine Keck AMS laboratories, and the University of Minnesota Institute of Rock Magnetism (which also provided a visiting fellowship for collection of rock magnetic data from EW0408-85JC). We also thank Bernie Housen, Elizabeth Patterson, and Robert Hatfield for facilitating and collecting additional hysteresis data from EW0408-85JC at Western Washington University. This work was supported by NSF grants EAR-0711584 (JSS, ACM), OCE-0351043 (Jaeger).

7 References

Addison, J.A., B.P. Finney, W.E. Dean, M.H. Davies, A.M. Mix, and J.M. Jaeger (2012), Productivity maxima and sedimentary $\delta^{15}N$ during the Last Glacial Maximum termination in the Gulf of Alaska, *Paleoceanography*, 27(1) doi:10.1029/2011/PA002161.

Amit, H. and P. Olson (2008), Geomagnetic Dipole Tilt Changes Induced by Core Flow, Physics of the Earth and Planetary Interiors, doi:10.1016/j.pepi.2008.01.007.

Amit, H., M. Korte, J. Aubert, and G. Hulot, (2011), The time-dependence of intense archeomagnetic flux patches, *Journal of Geophysical Research*, 116, B12106.

Aubert, J., C. Finlay, and A. Fournier (2013), Bottom-up control of geomagnetic secular variation by the Earth's inner core, *Nature*, 502, 219-223.

Barclay, D.J., E.M. Yager, J. Graves, M. Kloczko, and P.E. Calkin (2013), Late Holocene glacial history of the Copper River Delta, coastal south-central Alaska, and controls on valley glacier fluctuations, *Quaternary Science Reviews,* 81, 74-89.

Barletta, F., G. St-Onge, J.S. Stoner, P. Lajeunesse, and J. Locat (2010), A high-resolution

Holocene paleomagnetic secular variation and relative paleointensity stack from eastern Canada, *Earth and Planetary Science Letters,* 298, 162-174.

Bloemendal, J., J.W. King, F.R. Hall, and S.J. Doh (1992), Rock magnetism of Late Neogene and Pleistocene deep-sea sediments: relationship to sediment source, diagenetic processes, and sediment lithology, *Journal of Geophysical Research,* 97, 4361-4375.

Bloxham, J. (2002), Time-independent and time-dependent behaviour of high-latitude flux bundles at the core-mantle boundary, *Geophysical Research Letters*, 29, 1854, doi:10,1029/2001GBLO14543.

Bloxham, J., and D. Gubbins (1985), The secular variation of Earth's magnetic field, *Nature*, 317, 777-781.

Bloxham, J., and D. Gubbins (1987), Thermal core-mantle interactions, *Nature* 325, 511-513.

Cowan, E.A., S.A. Brachfeld, R.D. Powell, and S.C. Schoolfield (2006), Terrane-specific rock magnetic characteristics preserved in glacimarine sediment from southern coastal Alaska, *Canadian Journal of Earth Sciences,* 43, 1269-1282.

Cox, A. (1962), Analysis of the present geomagnetic field for comparison with paleomagnetic results, *Journal of Geomagnetisms and Geoelectricity,* 13, 35-51.

Creer, K. M., P. Tucholka (1982), Secular variation as recorded in lake sediments: a discussion of North American and European results, Phil. Trans. R. Soc. Lond. A 306, 87-102.

Davies, C.J., D. Gubbins, A.P. Willis, and P.K. Jimack (2008), Time-averaged paleomagnetic field and secular variation: Predictions from dynamo solutions based on lower mantle seismic tomography, *Physics of the Earth and Planetary Interiors,* 169, 194-203.

Davies, M.H., A.C. Mix, J.S. Stoner, J.A. Addison, J. Jaeger, B. Finney, J. Wiest, (2011) The deglacial transition on the Southeastern Alaska Margin: meltwater input, sealevel rise, marine productivity, and sedimentary anoxia, *Paleoceanography,* doi:10.1029/2010PA002051

Davies-Walczak, M.H., A.C. Mix, J.S. Stoner, J. Southon (2014), The flooding of Beringia and the onset of North Pacific Intermediate Water formation, *Earth and Planetary Science Letters* 397:57-66.

Day, R., M. Fuller, and V.A. Schmidt (1977), Hysteresis properties of titanomagnetites: Grain size and composition dependence, Physics of the Earth and Planetary Interiors, 13, 260-267.

Dunlop, D.J., 2002. Theory and application of the Day plot (Mrs/Ms versus Hcr/Hc) 1. Theoretical curves and tests using titanomagnetite data. Journal of Geophysical Research 107, 2056.

Gallet, Y., A. Genevey, and M. Le Goff (2002), Three millennia of directional variation of the Earth's magnetic field in Western Europe as revealed by archeological artifacts, *Physics of the Earth and Planetary Interior*, 131, 81-89.

Gallet, Y., G. Hulot, A. Chulliat, A. Genevey (2009), Geomagnetic field hemispheric asymmetry and archeomagnetic jerks, *Earth and Planetary Science Letters,* 284, 179-186.

Gallet, Y., M.M. Montaña, A. Genevey, X.C. García, E. Thébault, A.G. Bach, M. Le Goff, B. Robert, I. Nachasova (2015), New Late Neolithic (*c.* 7000-5000 BC) archeointensity data from Syria. Reconstructing 9000 years of archeomagnetic field intensity variations in the Middle East, *Physics of the Earth and Planetary Interiors,* 238, 89-103.

Geiss, CE, and SK Banerjee (2003), A Holocene–Late Pleistocene geomagnetic inclination record from Grandfather lake, SW Alaska, *Geophysical Journal International,* 153, 497-507.

Genevey, A. Y. Gallet, C.G. Constable, M. Korte, and G. Hulot (2008), ArcheoInt: An upgraded compilation of geomagnetic field intensity data for the past ten millennia and its application to the recovery of the past dipole moment, *Geochemistry Geophysics Geosystems,* doi:10.1029/2007GC001881

Gubbins, D., A.P. Willis, B. Sreenivasan (2007), Correlation of Earth's magnetic field with lower mantle thermal and seismic structure, *Physics of the Earth and Planetary Interiors*, 162, 256-260.

Hagstrum, J.T., and D.E. Champion (2002), A Holocene paleosecular variation record from 14C-dated volcanic rocks in western North America, *Journal of Geophysical Research*, 107(B1), 2025, doi:10.1029/2001JB000524.

Hagstrum, J.T., and E. Blinman (2010), Archeomagnetic dating in western North America: an updated reference curve based on paleomagnetic and archeomagnetic data sets, *Geochemistry, Geophysics, Geosystems,* 11, Q06009, doi:10.1029/2009/GC002979

Haslett, J. and A. Parnell (2008), A simple monotone process with application to radiocarbon-dated depth chronologies, *Journal of the Royal Statistical Society: Series C (Applied Statistics)*, 57(4), 399-418.

Herrero-Bervera H, and J-P. Valet, (2007). Holocene paleosecular variation from dated lava flows on Maui (Hawaii). Physics of the Earth and Planetary Interiors 161, 267–280

Jackson, A., A.R.T. Jonkers, and M.R. Walker (2000), Four centuries of geomagnetic

secular variation from historical records, *Philosophical Transactions of the Royal Society of London. Series A: Mathematical, Physical and Engineering Sciences,* 358, 957-990.

Jackson, M., Moskowitz, B.M., and Bowles, J. (2011). Interpretation of low-Temperature Data Part III: The Magnetite Verwey Transition (Part A). The IRM Quarterly, 20 (4) 1-11. ISSN: 2152-1972.

Jaeger, J.M., and C.A. Nittrouer (2006), A quantitative examination of modern sedimentary lithofacies formation on the glacially influenced Gulf of Alaska continental shelf, *Continental Shelf Research,* 26, 2178-2204.

Jaeger, J.M., C.A. Nittrouer, N.D. Scott, and J.D. Milliman (1998), Sediment accumulation along a glacially impacted mountainous coastline: Northeast Gulf of Alaska, *Basin Research,* 10, 155-173.

Karlin, R., and S. Levi (1983), Diagenesis of magnetic minerals in recent haemipelagic sediments, *Nature,* 303, 327-330.

King, J., S.K. Banerjee, J. Marvin, and O. Ozdemir (1982), A comparison of different magnetic methods for determining the relative grain size of magnetite in natural materials: some results from lake sediments, *Earth and Planetary Science Letters,* 59, 404-419.

Kirschvink, J.L. (1980), The least-squares line and plane and the analysis of palaeomagnetic data, *Geophysical Journal of the Royal Astronomical Society,* 62, 699-718.

Korte, M., and C.G. Constable (2005), Continuous geomagnetic field models for the past 7 millennia: 2, CALS7K*, Geochemistry, Geophysics, Geosystems,* 6, Q02H16, doi:10.1029/2004GC000801

Korte, M., C. Constable, F. Donadini, and R. Holme, (2011), Reconstructing the Holocene geomagnetic field, *Earth and Planetary Science Letters*, 312, 497-505.

Korte, M., F. Donadini, and C.G. Constable (2009), The geomagnetic field for 0-3 ka, Part II: a new series of time-varying global models, *Geochemistry, Geophysics, Geosystems,* 10, Q06008, doi:10.1029/2008GC002297

Korte, M., and R. Holme (2010), On the persistence of geomagnetic flux lobes in global Holocene field models, Physics of the Earth and Planetary Interiors, 182, 179-186.

Lisé-Pronovost, A., G. St-Onge, S. Brachfeld, F. Barletta, and D. Darby (2009), Paleomagnetic constraints on the Holocene stratigraphy of the Arctic Alaskan margin, *Global and Planetary Change,* 68, 85-99.

Lund, S.P. (1996), A comparison of Holocene paleomagnetic secular variation records

from North America, *Journal of Geophysical Research,* 101, 8007-8024.

Lund, S.P., and S.K. Banerjee (1985), Late Quaternary paleomagnetic field secular variation from two Minnesota lakes, *Journal of Geophysical Research,* 90(B1), 803-825.

Mazaud, A. (2005), User-friendly software for vector analysis of the magnetization of long sediment cores, *Geochemistry Geophysics Geosystems,* 6, Q12006, doi:10.1029/2005GC001036.

McNeely, R., A.S. Dyke, and J.R. Southon (2006), Canadian marine reservoir ages, preliminary data assessment, *Geological Survey Canada, Open File* 5049

Merrill, R., M. McElhinny, and P. McFadden (1996), *The Magnetic Field of the Earth*, Academic Press, San Diego, CA, 531 pp.

Nilsson, A., I. Snowball, R. Muscheler, and C. Bertacchi Uvo (2010), Holocene geocentric dipole tile model constrained by sedimentary paleomagnetic data, *Geochemistry Geophysics Geosystems,* 11, doi: 10.1029/2010GC003118.

Nilsson A., R. Muscheler, and I. Snowball (2011), Millennial scale cyclicity in the geodynamo inferred from a dipole tilt reconstruction, *Earth and Planetary Science Letters,* 311(3), 299-305.

Nilsson A., R. Holme, M. Korte, N. Suttie, M. Hill (2014), Reconstructing Holocene geomagnetic field variation: new methods, models, and implications (2014), *Geophysical Journal International*, doi: 10.1093/gji/ggu120 .

Özdemir, Ö., and D. J. Dunlop, (1996). Thermoremanence and Neel Temperature of Geothite. Geophysical Research Letters, 23, 921-924.

Özdemir, Ö., and D. J. Dunlop, 2010. Hallmarks of maghemitization in low-temperature cycling of partially oxidized magnetite nanoparticles. *J. Geophys. Res.,* 114, 10.1029/2009JB006756

Özdemir, Ö., and W. O'Reilly, 1981. High temperature hysteresis and other magnetic properties of synthetic monodomain titanomagnetites. Phys. Earth Planet. Inter., 25, 406-418.

Peng, L., and J.W. King (1992), A late Quaternary geomagnetic secular variation record from Lake Waiau, Hawaii, and the question of the Pacific nondipole low, *J. of Geophys. Res.,* 97(B2), 4407-4424.

Roberts, A. P., L. Chang, D. Heslop, F. Florindo, and J. C. Larrasoana (2012), Searching for single domain magnetite in the 'pseudo-single-domain' sedimentary haystack: Implications of biogenic magnetite preservation for sediment magnetism and relative paleointensity determinations, *J. Geophys. Res.*, doi:10.1029/2012JB009412.

Sambrotto, R.N., and C.J. Lorenzen (1987), Phytoplankton and primary production, in *The Gulf of Alaska,* Edited by Hood, D.W., and S.T. Zimmerman, pp. 249-282, U.S. Department of Commerce, USA.

Stoner, J.S. and G. St-Onge (2007), Magnetic stratigraphy: Reversals, excursions, paleointensity and secular variation, in *Development in Marine Geology: Volume 1, Proxies in Late-Cenezoic Paleoceanography,* Edited by Hillaire-Marcel, C., and A. de Vernal, pp. 99-138.

Stoner, J.S., J.E.T. Channell, A. Mazaud, C. Xuan, and S. E. Strano, *2013*: The influence of high latitude flux lobes on the Holocene paleomagnetic record of IODP Site U1305 and the northern North Atlantic. *Geochemistry, Geophysics, Geosystems,* 14, 4623-4646, 10.1002/ggge.20272.

Stuiver, M., and P.J. Reimer (1993), Extended 14C database and revised CALIB radiocarbon calibration program, *Radiocarbon,* 35, 137-189.

Tarduno, J.A., W. Tian, S. Wilkison (1998) Biogeochemical remanent magnetization in pelagic sediments of the western equatorial Pacific Ocean (2013), *Geophysical Research Letters*, 25, 3987-3990.

Tarduno, J.A., and S.L. Wilkison (1996), Non-steady state magnetic mineral reduction, chemical lock-in, and delayed remanence acquisition in pelagic sediments, *Earth and Planetary Science Letters, 144*, 315-326.

Tauxe, L. (1993), Sedimentary records of relative paleointensity of the geomagnetic field: theory and practice, *Reviews of Geophysics,* 31, 319-354.

Tauxe, L., (1998), *Paleomagnetic Principles and Practice*, Dordrecht, The Netherlands: Kluwer Academic Publishers

Thomas, R.G., Y. Guyodo, and J.E.T. Channell (2003), U-channel track for susceptibility measurements, *Geochemistry, Geophysics, Geosystems,* 4, doi:10.1029/2002GC000454.

Thompson, R. (1984), Geomagnetic evolution: 400 years of change on planet earth, *Physics of the Earth and Planetary Interiors*, 36(1), 61-77.

Verosub, K.L., P.J. Mehringer Jr, and P. Waterstraat (1986), Holocene secular variation in western North America: paleomagnetic record from Fish Lake, Harney County, Oregon, *Journal of Geophysical Research,* 91, 3609-3623.

Verwey, E. J. (1939), Electronic conduction of magnetite (Fe3O4) and its transition point at low temperature, *Nature*, 144, 327-328.

Walinsky, S.E., F.G. Prahl, A.C. Mix, B.P. Finney, J.M. Jaeger, and G.P. Rosen (2009),

Distribution and composition of organic matter in surface sediments of coastal Southeast Alaska, *Continental Shelf Research*, 29(13), 1565-1579.

Weeks, R.J., C. Laj, L. Endignoux, M.D. Fuller, A.P. Robert, R. Manganne, E. Blanchard, and W. Goree (1993), Improvements in long core measurement techniques: applications in paleomagnetism and paleoceanography, *Geophysical Journal International*, 114, 651–662.

Weingartner, K. Coyle, B. Finney, R. Hopcroft, T. Whitledge, R. Brodeur, M. Dagg, E. Farley, D. Haidvogel, L. Haldorson, A. Hermann, S. Hinckley, J. Napp, P. Stabeno, T. Kline, C. Lee, E. Lessard, T. Royer and S. Strom (2002), The Northeast Pacific GLOBEC Program: Coastal Gulf of Alaska, *Oceanography,* 15(2), 10–35.

Wiles, G.C., D.J. Barclay, P.E. Calkin, and T.V. Lowell, (2008). Century to millennial-scale temperature variations for the last two thousand years inferred from glacial geologic records of southern Alaska, *Global and Planetary Change,* 60, 115–125. doi:10.1016/j.gloplacha.2006.07.036.

Figure Captions

Figure 1: Site map showing the bathymetry of the Gulf of Alaska, as well as the locations of shelf core EW0408-79JC and slope core EW0408-85JC. The locations of the major sediment sources to the margin, which include drainages from the Bering and Malaspina glaciers as well as the Copper River, are labeled.

Figure 2: a) Computerized tomographic (CT) scan of EW0408-79JC, shown in false color to highlight density changes. Warmer (green, yellow) colors indicate high densities associated with larger lithogenic grains, while cooler (blue, purple) colors indicate lower densities associated with finer clays and biogenic sedimentation. The massive sandy-silt deposit excluded from paleomagnetic interpretation (575-705 cmbsf) is indicated in orange. **b)** The section below 1350 cmbsf in the core shows vertical flow structures meters in scale, indicative of extreme coring deformation. **c)** Computerized tomographic (CT) scan of EW0408-85JC, shown in false color to highlight density changes (Davies et al., 2011). Warmer (green, yellow) colors indicate high densities associated with larger lithogenic grains, while cooler (blue, purple) colors indicate lower densities associated with finer clays and biogenic sedimentation. **d)** The deglacial transition is characterized by abrupt shifts in lithology, as well as intermittent laminae preservation associated with high organic carbon content and low bottom water oxygen content.

Figure 3: Calibrated planktonic foraminiferal dates used to generate the age models for EW0408-79JC (blue circles) and EW0408-85JC (red diamonds). Plotted error bars on individual dates and the error windows of the age models represent 1-sigma uncertainty.

Figure 4: Bulk magnetic parameters from EW0408-79JC, indicating natural remanent magnetization (NRM) intensities for AF-demagnetization steps from 0-100 mT,

component inclinations (GAD prediction = 74°, shown as dashed line), declinations, and mean angular deviation (MAD) values calculated from the 10-60 mT steps, magnetic susceptibility, laboratory-applied anhysteretic (ARM) and 0.3 T isothermal (IRM) remanent magnetization intensities for AF-demagnetization steps from 0-80 mT, the down-core k_{ARM}/k ratio, and sediment accumulation rates derived from the planktonic radiocarbon dates (red triangles). The massive sandy-silt deposit excluded from paleomagnetic interpretation (575-705 cmbsf) is indicated in orange.

Figure 5: Bulk magnetic parameters from EW0408-85JC, indicating natural remanent magnetization (NRM) intensities for AF-demagnetization steps from 0-100 mT, component inclinations (GAD prediction = 74°, shown as dashed line), declinations, and mean angular deviation (MAD) values calculated from the 10-60 mT steps, magnetic susceptibility, laboratory-applied anhysteretic (ARM) and 0.3 T isothermal (IRM) remanent magnetization intensities for AF-demagnetization steps from 0-80 mT, the down-core k_{ARM}/k ratio, and sediment accumulation rates derived from the planktonic radiocarbon dates (red triangles).

Figure 6: Rock magnetic measurements on selected samples from EW0408-85JC including a) hysteresis ratios Mrs/Ms vs. Hcr/Hc presented in the form of a Day et al., (1977) diagram (samples from the weakly magnetized interval between 710-850 cmbsf denoted with solid red symbols) b) backfield experiments normalized to the magnetization 0 T, c) thermal demagnetization curves normalized to remanence at room temperature (~22-25°C) and d) low-temperature SIRM experiments normalized to remanence at starting temperature (300 K). Note that Ms/T data is unavailable from 649 cmbsf, and LTRTSIRM data is unavailable from 777.5 cmbsf.

Figure 7: Component Inclinations, Declinations, and Normalized Remanence (NRM/ARM @ 30mT demagnetization) from EW0408-85TC/JC (red/pink) and EW0408-79JC (orange; 100-year smoothed record shown in bold), superimposed on the site predictions from the Holocene CALS7K.2 (light gray, *Korte and Constable, 2005*), CALS10k.b (light blue, Korte et al., 2009, 2011), FBNKE (dark gray, Nilsson et al., 2010) and historic GUFM1 (dark green, *Jackson et al., 2000*) field models.

Figure 8: North Pacific Holocene inclination records, compared on independent chronologies. From left to right: Lake Waiau, Hawaii (solid purple line, *Peng and King, 1992*), Fish Lake (solid pink line, *Verosub et al.,* 1986), Gulf of Alaska record EW0408-85TC/JC (dashed/solid red line), and Grandfather Lake, Alaska (hollow black diamonds, *Geiss and Banerjee, 2003*). GAD predicted inclination values are shown as a solid line for each record. A stack of these North Pacific inclination records was generated by adjusting each record to deviation from its GAD predicted value (ΔI) following interpolation to 100 year resolution and smoothing with a 300 year Gaussian filter, is shown in green. The number of records (N) available for each time step is shown to the left of the stack. Stacks generated from model inclination predictions for the same four sites are shown for CALS7K.2 (*light gray, Korte and Constable, 2005)*, CALS10k.b (light blue, Korte et al., 2009, 2011), and FBNKE (dark gray, Nilsson et al., 2010). Uncertainty windows shown reflect 1-σ error.

Figure 9: Comparison of stacked Northeast Pacific inclination deviations from their GAD-predicted values (green, plotted uncertainty 1-σ) with (from left to right) archeomagnetic inclinations from Western US volcanics (red; Hagstrum and Champion, 2002), archeomagnetic North American virtual axial dipole moments (VADM) (gray; Genevey et al., 2008), North Atlantic declination as determined via composite records from Greenland and Iceland (blue; Stoner et al., 2013), and Western European VADM (black; Genevey et al., 2008).

Figure 10: Comparison of stacked Northeast Pacific (NEPSIAS) inclination deviations from their GAD-predicted values (green) superimposed upon North Atlantic declination as determined via composite records from Greenland and Iceland (blue; Stoner et al., 2013), compared to (from left to right) virtual geomagnetic pole (VGP) longitude and latitude predictions from NEPSIAS (green) and field model FBNKE (Nilsson et al., 2010) and Western European VADM (black; Genevey et al., 2008).

Figure A.1: Point source magnetic susceptibility and gamma-ray attenuation density data illustrating generation of cmbsf scale for EW0408-79JC (**a, b**) and EW0408-79JC (**c, d**).

Figure A.2: a) Bulk magnetic parameters from EW0408-78MC7, indicating natural remanent magnetization (NRM) intensities for AF-demagnetization steps from 0-100 mT, component inclinations, declinations, and mean angular deviation (MAD) values calculated from the 10-60 mT steps, magnetic susceptibility, laboratory-applied anhysteretic (ARM) and 0.3 T isothermal (IRM) remanent magnetization intensities for AF-demagnetization steps from 0-80 mT, and the down-core k_{ARM}/k ratio. **b)** The above properties measured for EW0408-79TC, as well as accumulation rates derived from radiocarbon dates on equivalent depths in associated jumbo piston core EW0408-79JC.

Figure A.3: a) Bulk magnetic parameters from EW0408-84MC8, indicating natural remanent magnetization (NRM) intensities for AF-demagnetization steps from 0-100 mT, component inclinations, declinations, and mean angular deviation (MAD) values calculated from the 10-60 mT steps, magnetic susceptibility, laboratory-applied anhysteretic (ARM) and 0.3 T isothermal (IRM) remanent magnetization intensities for AF-demagnetization steps from 0-80 mT, and the down-core k_{ARM}/k ratio. **b)** The above properties measured for EW0408-85TC, as well as accumulation rates derived from radiocarbon dates in the core (red triangles).

Figure A.4: Component inclinations and declinations, as well as mean angular deviation (MAD) values calculated using the 10-60 mT AF demagnetization steps (gray, pink), as well as using the optimized demagnetization step selection approach described in the text (black, red). S-ratio values indicates that magnetite is the dominant remanence carrier in both EW0408-79JC (light blue) and EW0408-85JC (dark blue), however the increase in MAD values in the early Holocene and during deglaciation appears to be associated with an increase in the proportion of high-coercivity magnetic minerals.

Figure A.5 a) Paramagnetic slope-corrected hysteresis loops from select depths spanning

the range of lithologies present in EW0408-85JC, as well as **b)** the same loops normalized to the magnetization in a 1 T field. The loops are broadly consistent with a magnetite minerology, although the greater hysteresis loop widths in the weakly magnetic samples between 777.5-850 cmbsf potentially indicate finer magnetic grainsize and/or a high-coercivity contribution to remanence (i.e. hematite; Tauxe 1998).

Figure A.6: a) The remanence coercivity measured on discrete samples in EW0408-85TC/JC and **b)** median destructive field of NRM for EW0408-85JC (normalized to the 10mT demag step) indicates two intervals between 715 and 850 cmbsf dominated by a high-coercivity magnetic remanence carrier, approximately coeval in the sediment column with to **c**) two episodes of elevated primary productivity as indicated by elevated biogenic silica preservation (Davies et al., 2011; Addison et al., 2012).

Figure A.7: North Pacific Holocene declination records, rotated to a mean of 0° and compared on independent chronologies. From left to right: Lake Waiau, Hawaii (solid purple line, *Peng and King, 1992*), Fish Lake (solid pink line, *Verosub et al.,* 1986), and Gulf of Alaska record EW0408-85TC/JC (dashed/solid red line). A stack of these North Pacific declination records, following interpolation to 100 year resolution and smoothing with a 300 year Gaussian filter, is shown in green. The number of records (N) available for each time step is shown to the left of the stack. Stacks generated from model declination predictions for the same four sites (also rotated to a mean of 0°) are shown for CALS7K.2 (*light gray, Korte and Constable, 2005)*, CALS10k.b (light blue, Korte et al., 2009, 2011), and FBNKE (dark gray, Nilsson et al., 2010). Uncertainty windows shown reflect 1-σ error.

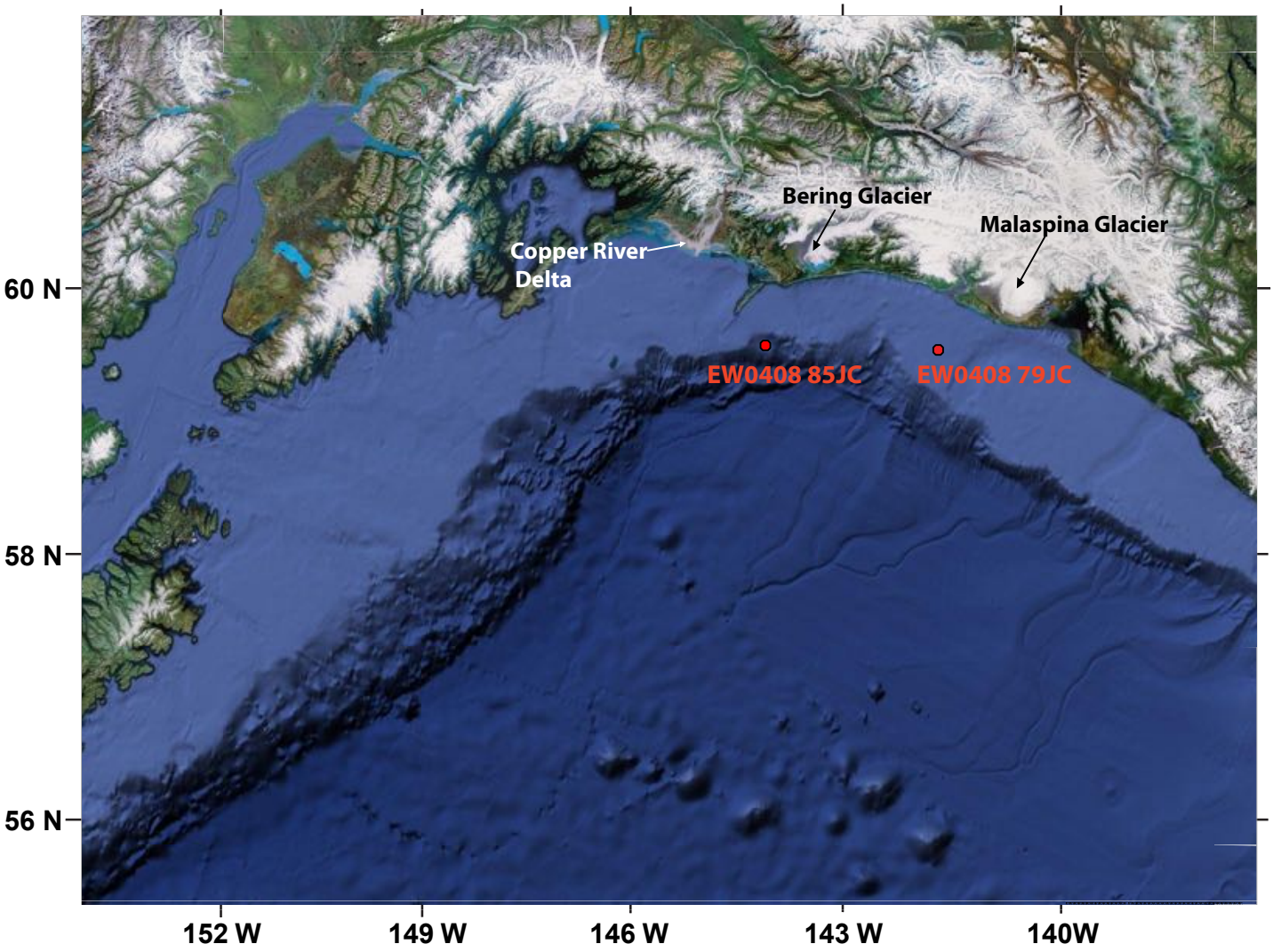
Bering Glacier
Malaspina Glacier
Copper River
Delta
EW0408 85JC
EW0408 79JC
60 N
58 N
56 N
152 W
149 W
146 W
143 W
140W

Figure A.1

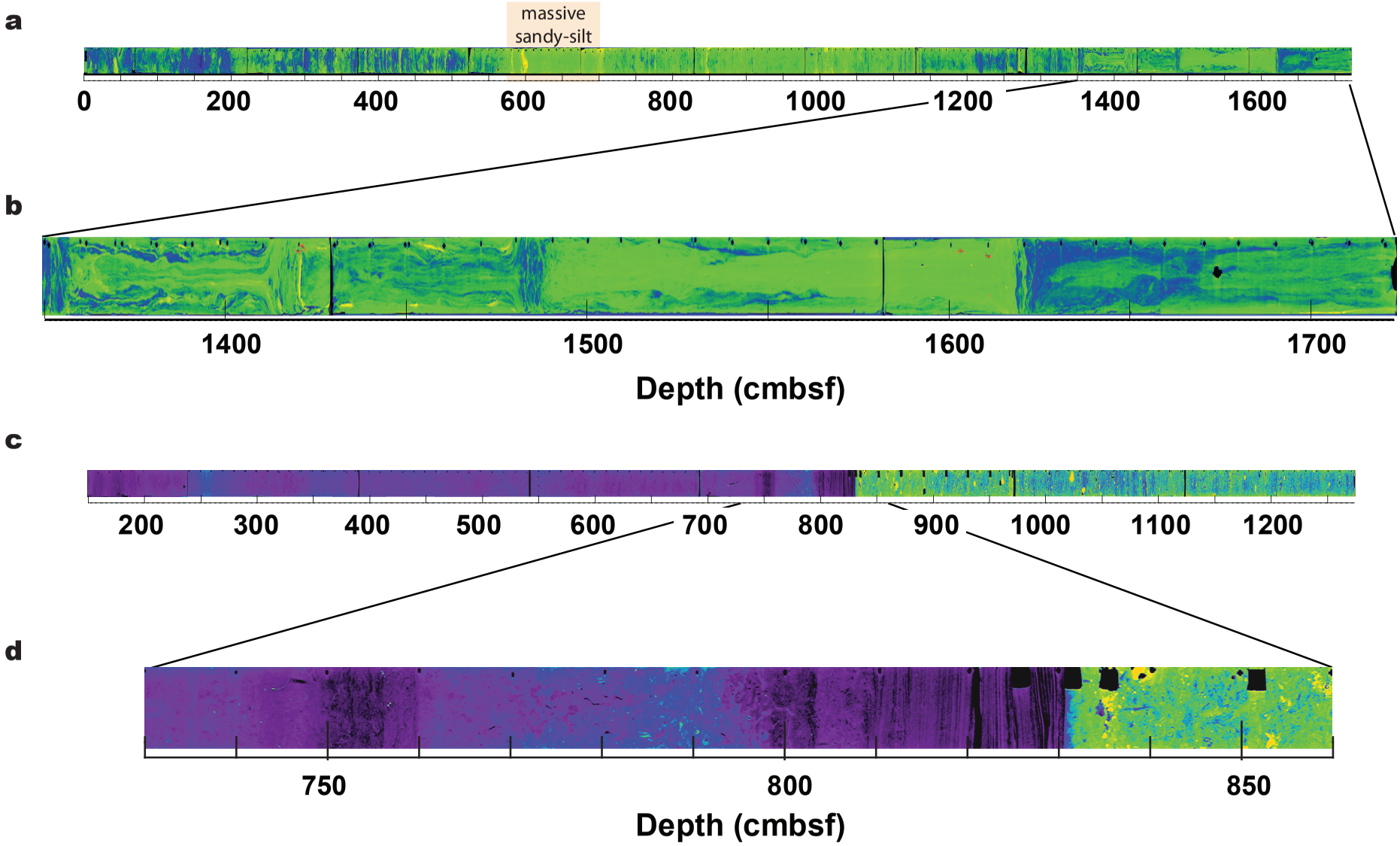
a
massive
sandy-silt
0
200
400
600
800
1000
1200
1400
1600
b
1400
1500
1600
1700
Depth (cmbsf)
c
200
300
400
500
600
700
800
900
1000
1100
1200
d
750
800
850
Depth (cmbsf)

Figure 2

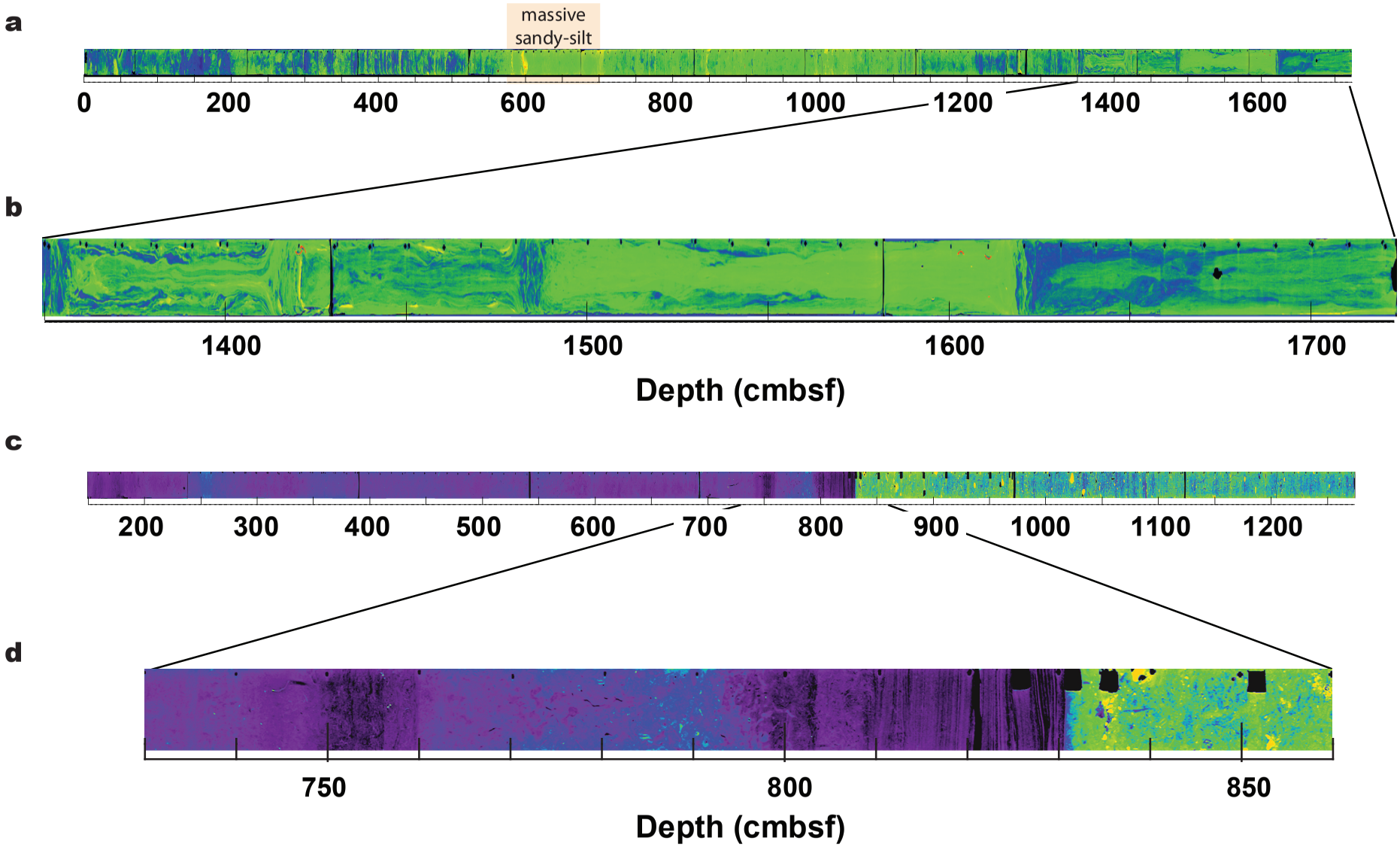
a
massive
sandy-silt
0
200
400
600
800
1000
1200
1400
1600
b
1400
1500
1600
1700
Depth (cmbsf)
c
200
300
400
500
600
700
800
900
1000
1100
1200
d
750
800
850
Depth (cmbsf)

Figure 2

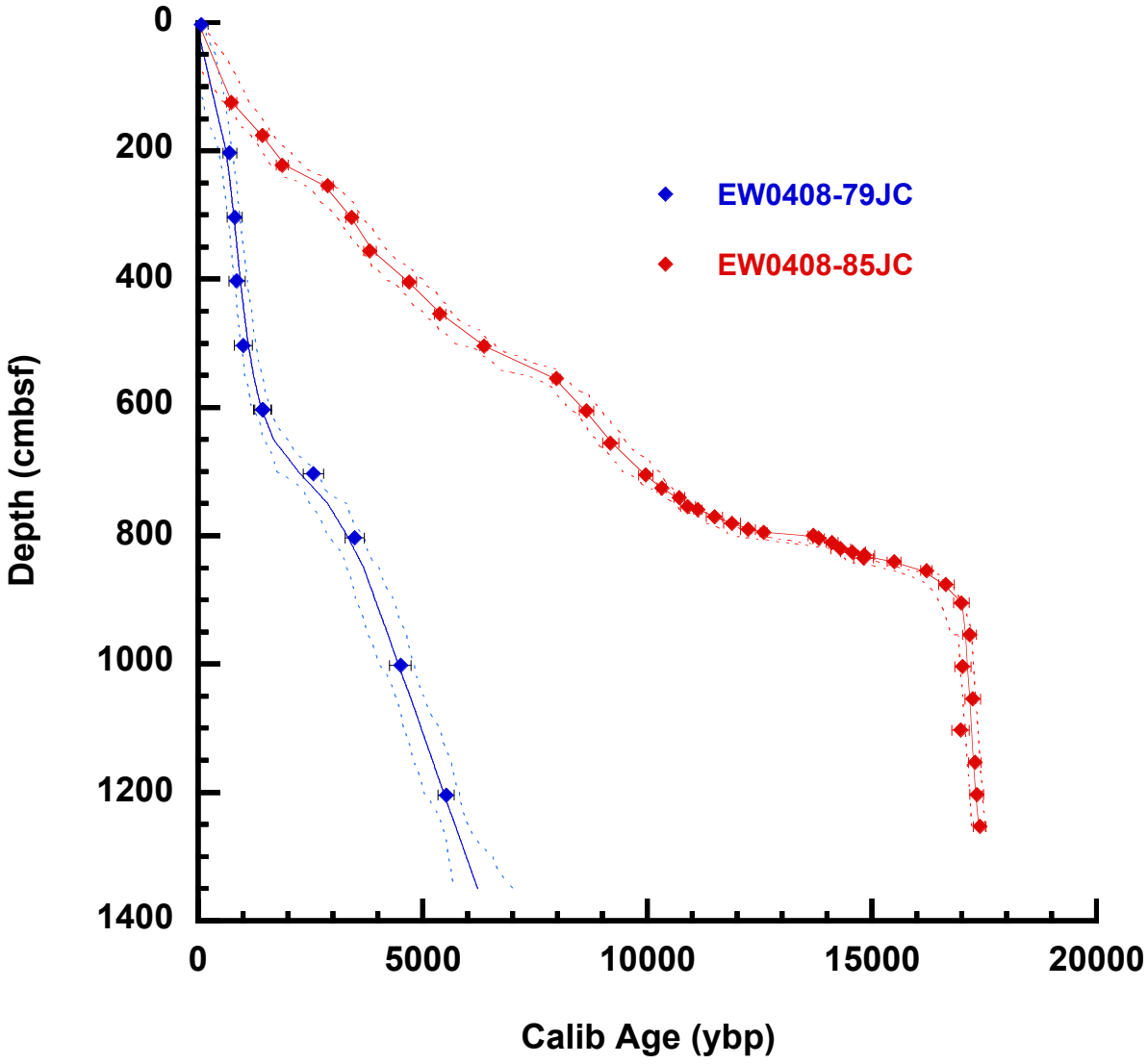
0
200
400
600
800
1000
1200
1400
Depth (cmbsf)
0
5000
10000
15000
20000
Calib Age (ybp)
EW0408-79JC
EW0408-85JC

Figure 3

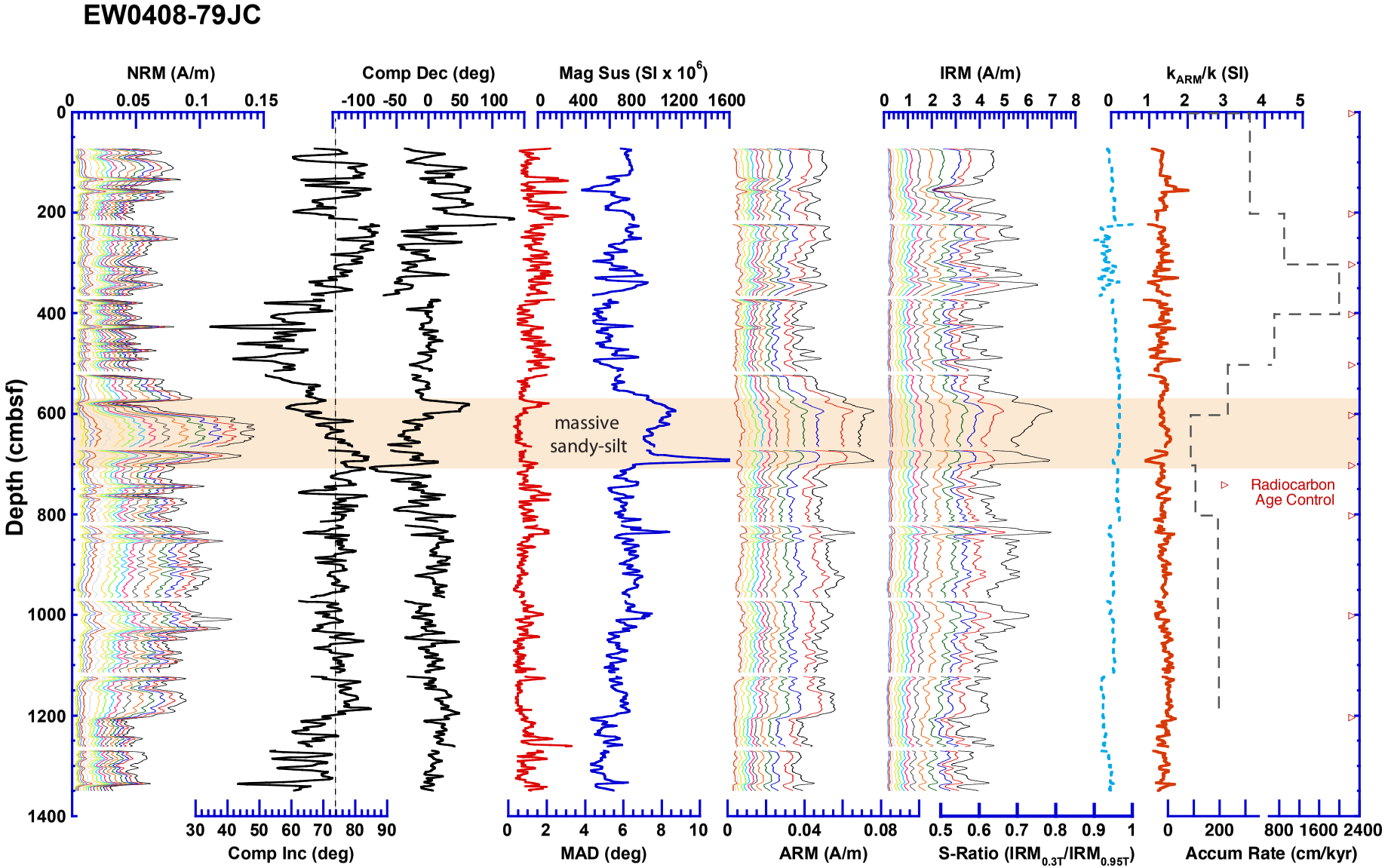
EW0408-79JC
NRM (A/m)
0 0.05 0.1 0.15
Comp Dec (deg)
-100 -50 0 50 100
Mag Sus (SI x 10^6)
0 400 800 1200 1600
IRM (A/m)
0 1 2 3 4 5 6 7 8
k_ARM/k (SI)
0 1 2 3 4 5
Depth (cmbsf)
0 200 400 600 800 1000 1200 1400
massive
sandy-silt
Radiocarbon
Age Control
30 40 50 60 70 80 90
Comp Inc (deg)
0 2 4 6 8 10
MAD (deg)
0 0.04 0.08
ARM (A/m)
0.5 0.6 0.7 0.8 0.9 1
S-Ratio (IRM0.3T/IRM0.95T)
0 200 800 1600 2400
Accum Rate (cm/kyr)

Figure 4

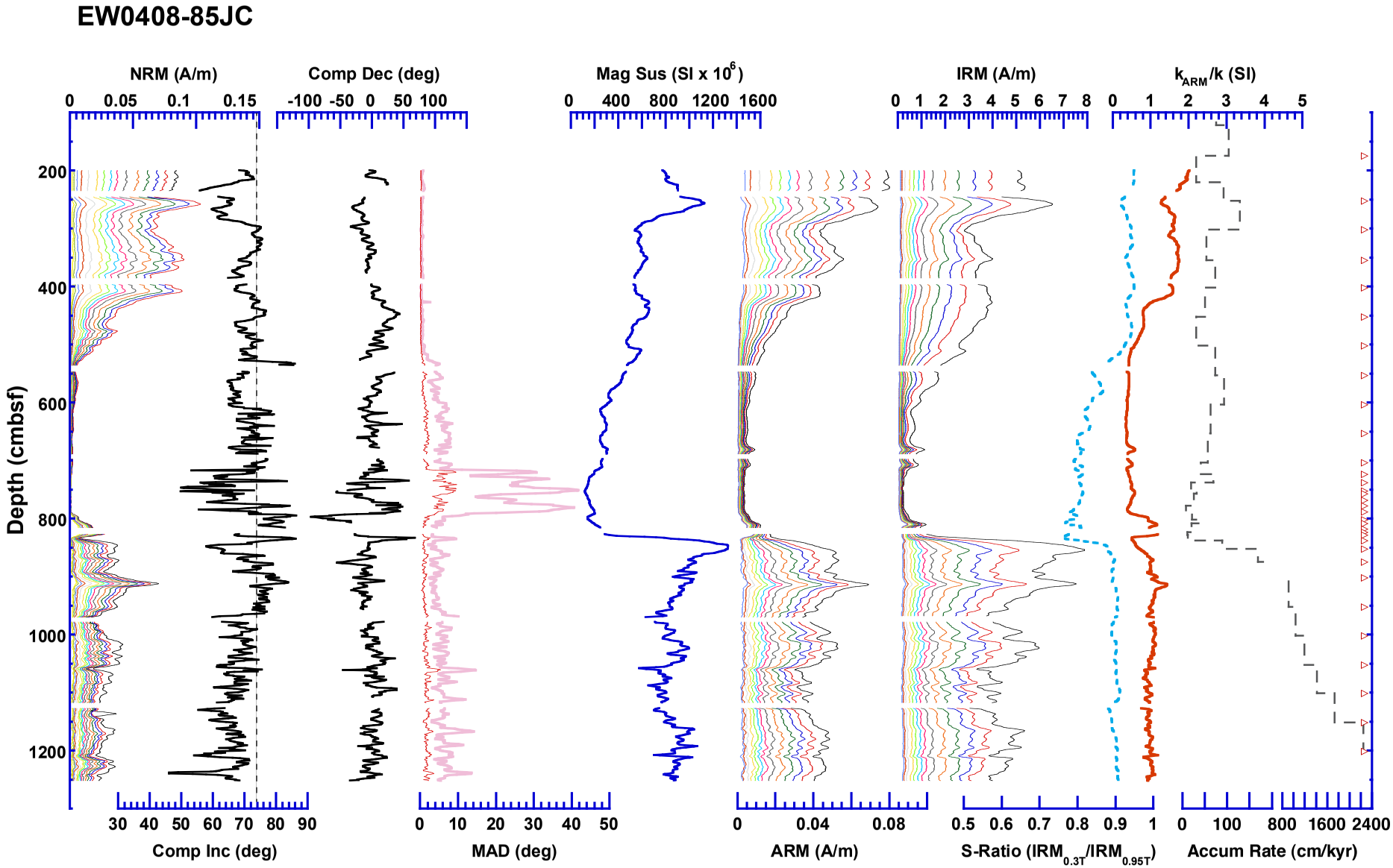
EW0408-85JC
NRM (A/m)
0 0.05 0.1 0.15
Comp Dec (deg)
-100 -50 0 50 100
Mag Sus (SI x 10^6)
0 400 800 1200 1600
IRM (A/m)
0 1 2 3 4 5 6 7 8
k_ARM/k (SI)
0 1 2 3 4 5
Depth (cmbsf)
200
400
600
800
1000
1200
30 40 50 60 70 80 90
Comp Inc (deg)
0 10 20 30 40 50
MAD (deg)
0 0.04 0.08
ARM (A/m)
0.5 0.6 0.7 0.8 0.9 1
S-Ratio (IRM0.3T/IRM0.95T)
0 100 800 1600 2400
Accum Rate (cm/kyr)

Figure 5

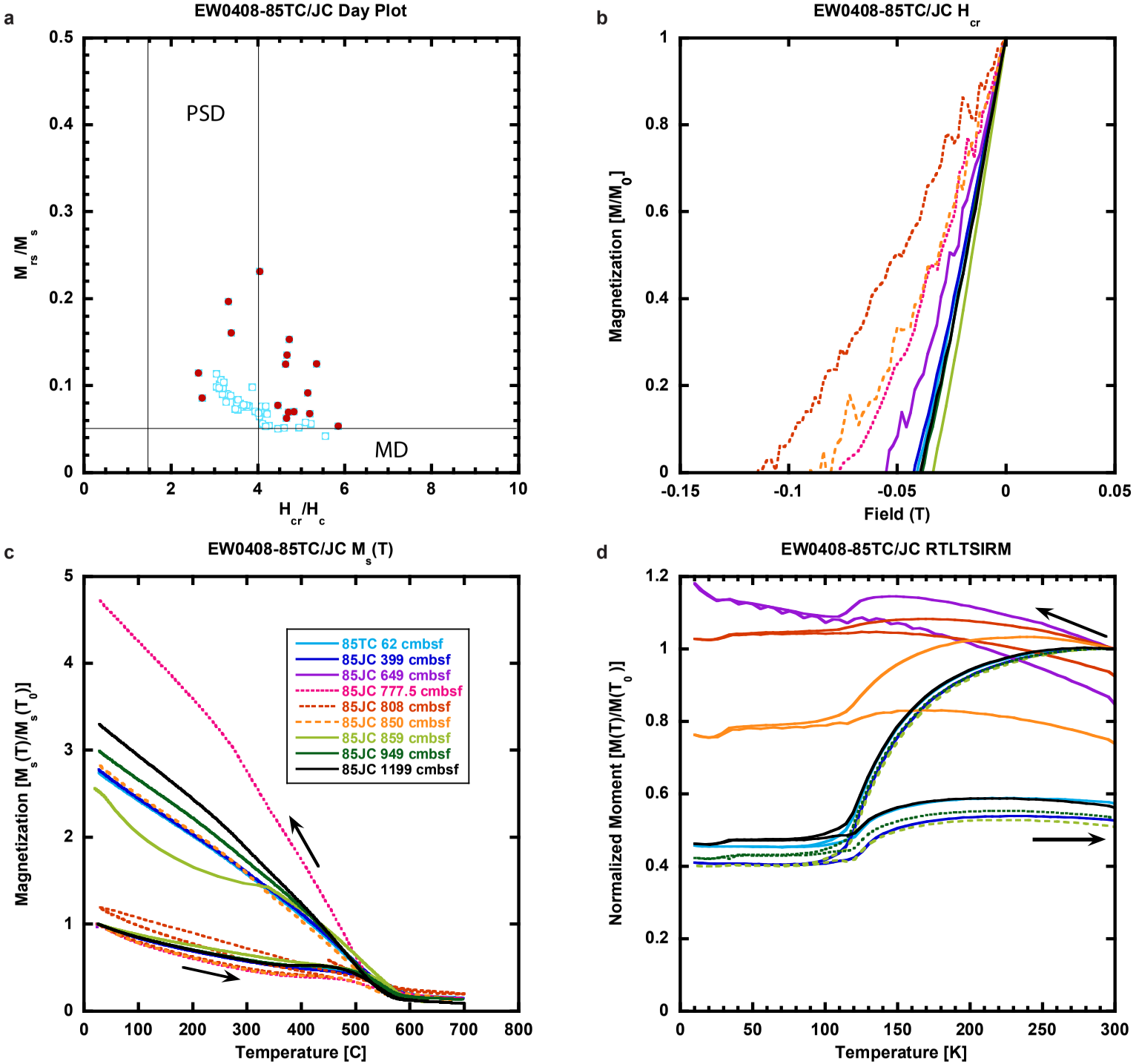
a
EW0408-85TC/JC Day Plot
PSD
MD
M_rs/M_s
H_cr/H_c
b
EW0408-85TC/JC H_cr
Magnetization [M/M_0]
Field (T)
c
EW0408-85TC/JC M_s(T)
85TC 62 cmbsf
85JC 399 cmbsf
85JC 649 cmbsf
85JC 777.5 cmbsf
85JC 808 cmbsf
85JC 850 cmbsf
85JC 859 cmbsf
85JC 949 cmbsf
85JC 1199 cmbsf
Magnetization [M_s(T)/M_s(T_0)]
Temperature [C]
d
EW0408-85TC/JC RTLTSIRM
Normalized Moment [M(T)/M(T_0)]
Temperature [K]

Figure 6

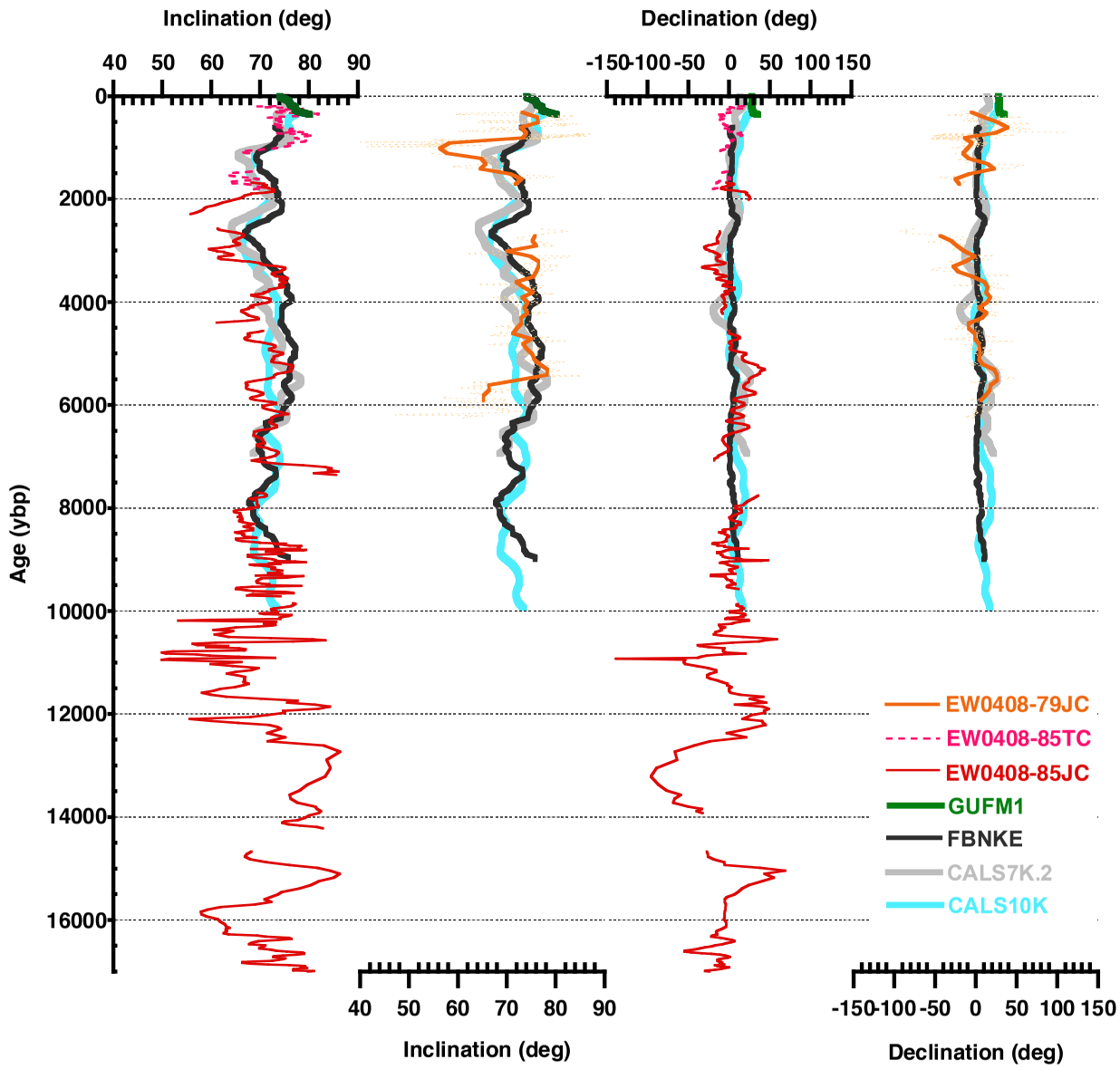
Inclination (deg)
40 50 60 70 80 90
Declination (deg)
-150 -100 -50 0 50 100 150
Age (ybp)
0
2000
4000
6000
8000
10000
12000
14000
16000
EW0408-79JC
EW0408-85TC
EW0408-85JC
GUFM1
FBNKE
CALS7K.2
CALS10K
40 50 60 70 80 90
Inclination (deg)
-150 -100 -50 0 50 100 150
Declination (deg)

Figure 7

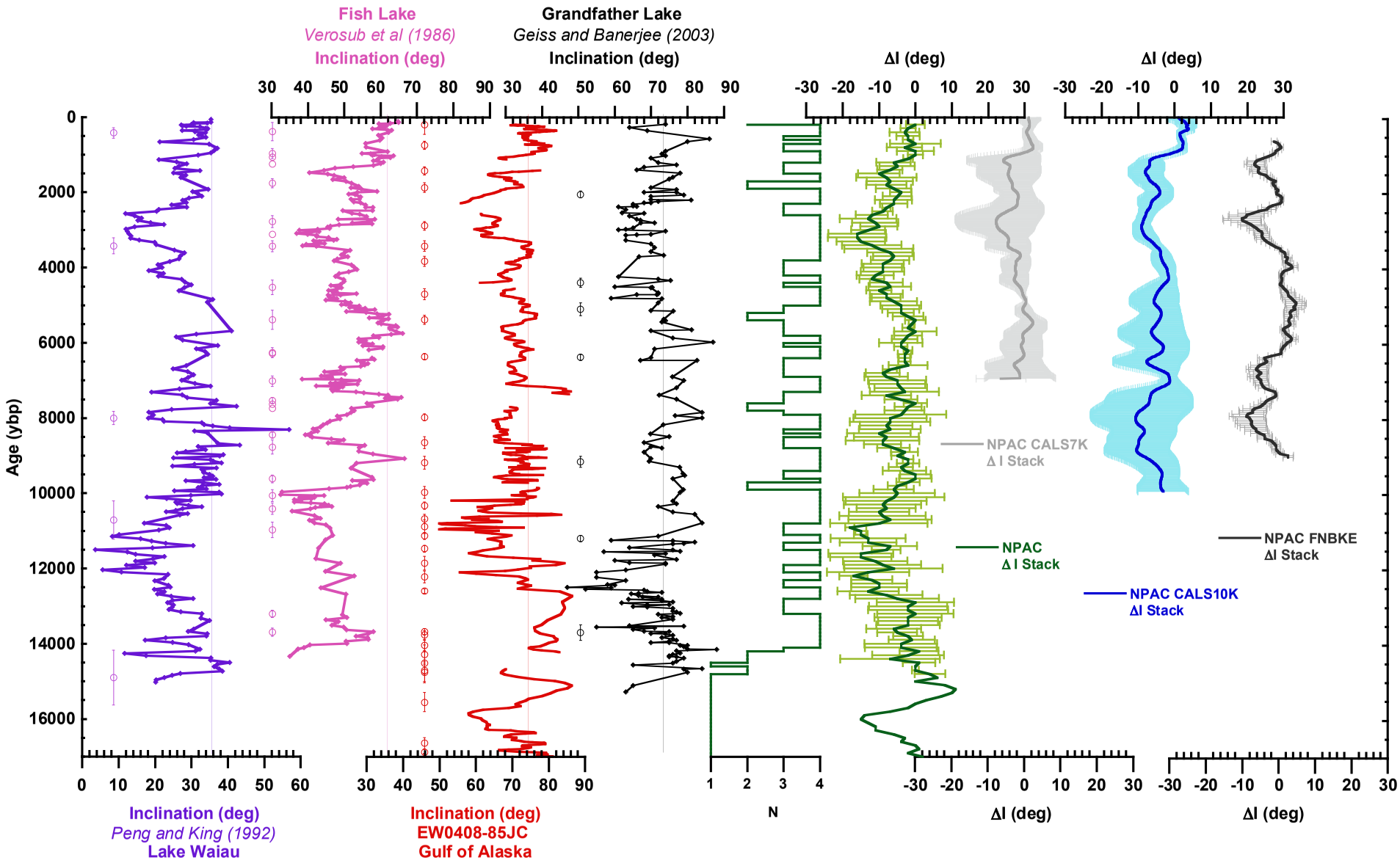
Fish Lake
Verosub et al (1986)
Inclination (deg)
Grandfather Lake
Geiss and Banerjee (2003)
Inclination (deg)
ΔI (deg)
ΔI (deg)
Age (ybp)
NPAC CALS7K
Δ I Stack
NPAC
Δ I Stack
NPAC CALS10K
ΔI Stack
NPAC FNBKE
ΔI Stack
Inclination (deg)
Peng and King (1992)
Lake Waiau
Inclination (deg)
EW0408-85JC
Gulf of Alaska
N
ΔI (deg)
ΔI (deg)

Figure 8

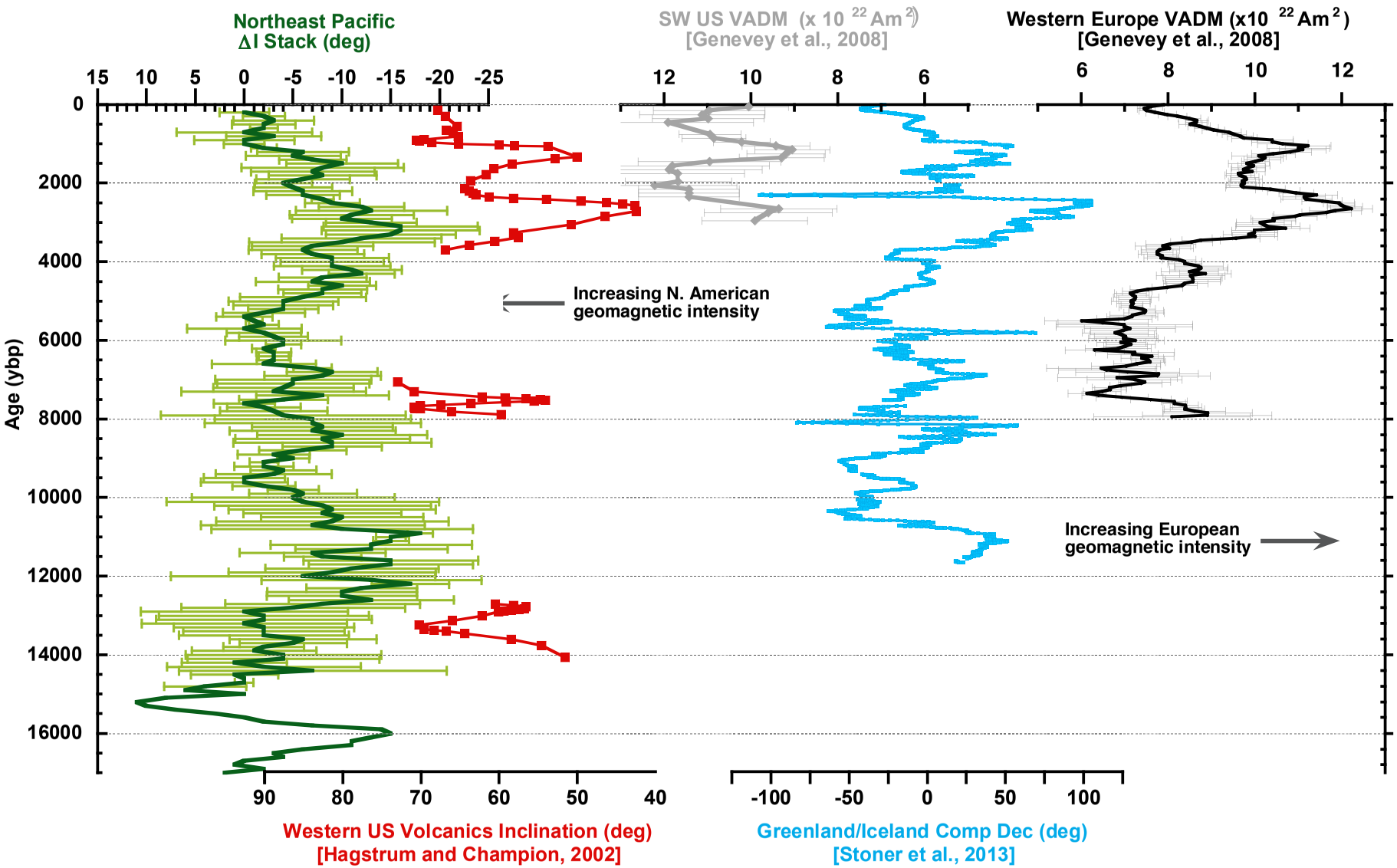
Northeast Pacific
ΔI Stack (deg)
SW US VADM (x 10 22 Am 2)
[Genevey et al., 2008]
Western Europe VADM (x10 22 Am 2)
[Genevey et al., 2008]
Age (ybp)
Increasing N. American
geomagnetic intensity
Increasing European
geomagnetic intensity
Western US Volcanics Inclination (deg)
[Hagstrum and Champion, 2002]
Greenland/Iceland Comp Dec (deg)
[Stoner et al., 2013]

Figure 9

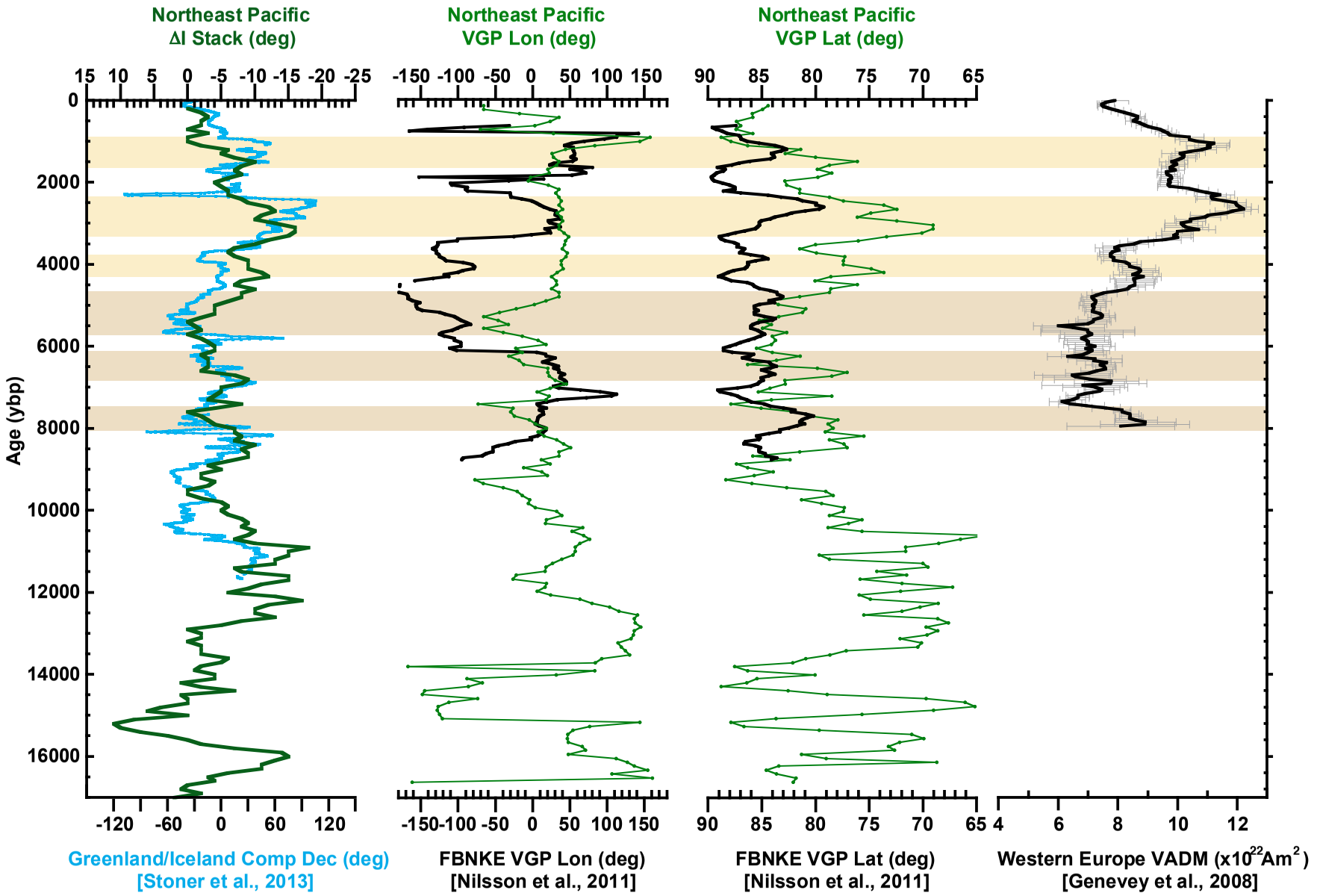
Northeast Pacific
ΔI Stack (deg)
Northeast Pacific
VGP Lon (deg)
Northeast Pacific
VGP Lat (deg)
15 10 5 0 -5 -10 -15 -20 -25
-150 -100 -50 0 50 100 150
90 85 80 75 70 65
Age (ybp)
0
2000
4000
6000
8000
10000
12000
14000
16000
-120 -60 0 60 120
-150 -100 -50 0 50 100 150
90 85 80 75 70 65
4 6 8 10 12
Greenland/Iceland Comp Dec (deg)
[Stoner et al., 2013]
FBNKE VGP Lon (deg)
[Nilsson et al., 2011]
FBNKE VGP Lat (deg)
[Nilsson et al., 2011]
Western Europe VADM (x10^22 Am^2)
[Genevey et al., 2008]

Figure 10

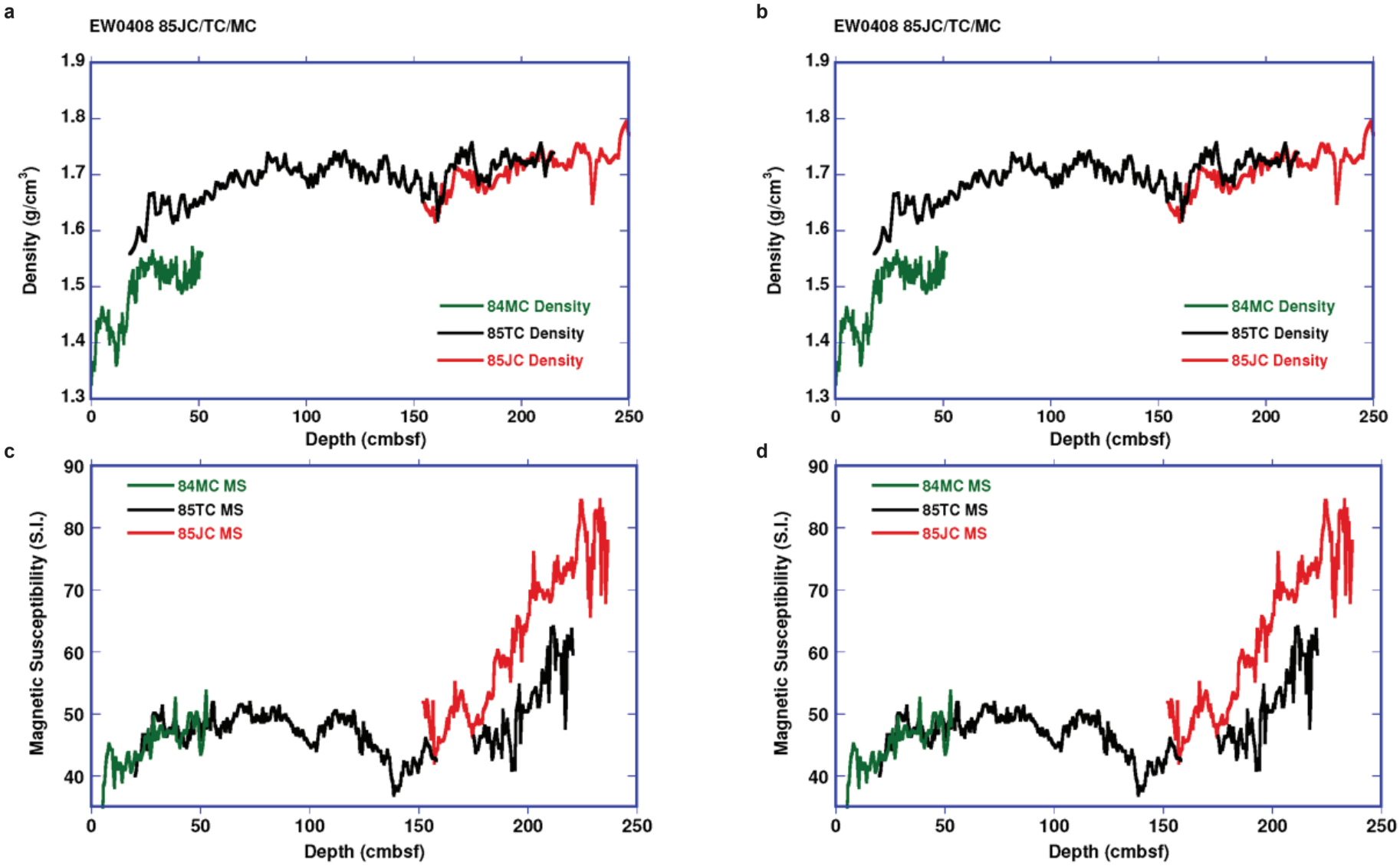
a
EW0408 85JC/TC/MC
Density (g/cm3)
Depth (cmbsf)
84MC Density
85TC Density
85JC Density
b
EW0408 85JC/TC/MC
Density (g/cm3)
Depth (cmbsf)
84MC Density
85TC Density
85JC Density
c
Magnetic Susceptibility (S.I.)
Depth (cmbsf)
84MC MS
85TC MS
85JC MS
d
Magnetic Susceptibility (S.I.)
Depth (cmbsf)
84MC MS
85TC MS
85JC MS

Figure A.1

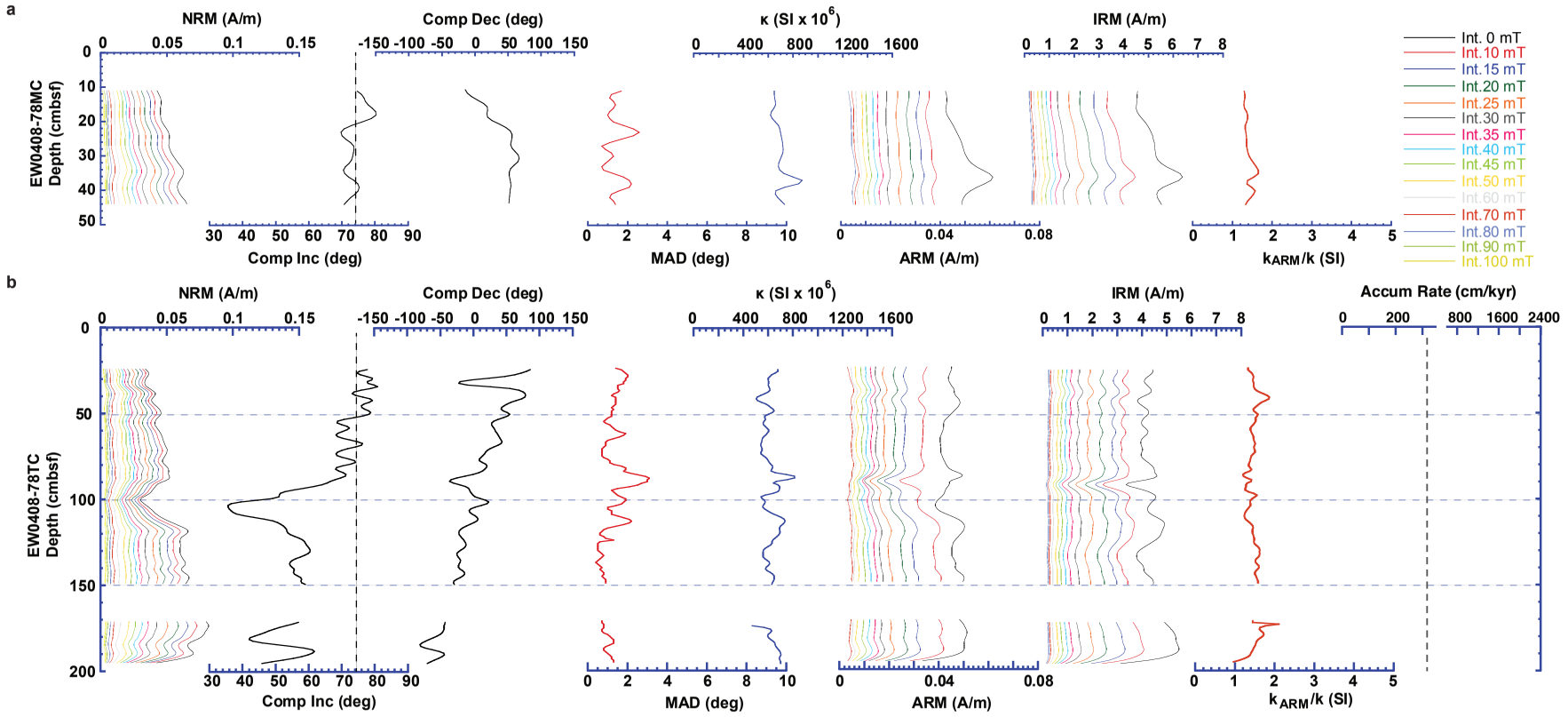
a
NRM (A/m)
Comp Dec (deg)
κ (SI x 10^6)
IRM (A/m)
EW0408-78MC Depth (cmbsf)
Comp Inc (deg)
MAD (deg)
ARM (A/m)
kARM/k (SI)
Int. 0 mT
Int.10 mT
Int.15 mT
Int.20 mT
Int.25 mT
Int.30 mT
Int.35 mT
Int.40 mT
Int.45 mT
Int.50 mT
Int.60 mT
Int.70 mT
Int.80 mT
Int.90 mT
Int.100 mT
b
NRM (A/m)
Comp Dec (deg)
κ (SI x 10^6)
IRM (A/m)
Accum Rate (cm/kyr)
EW0408-78TC Depth (cmbsf)
Comp Inc (deg)
MAD (deg)
ARM (A/m)
kARM/k (SI)

Figure A.2

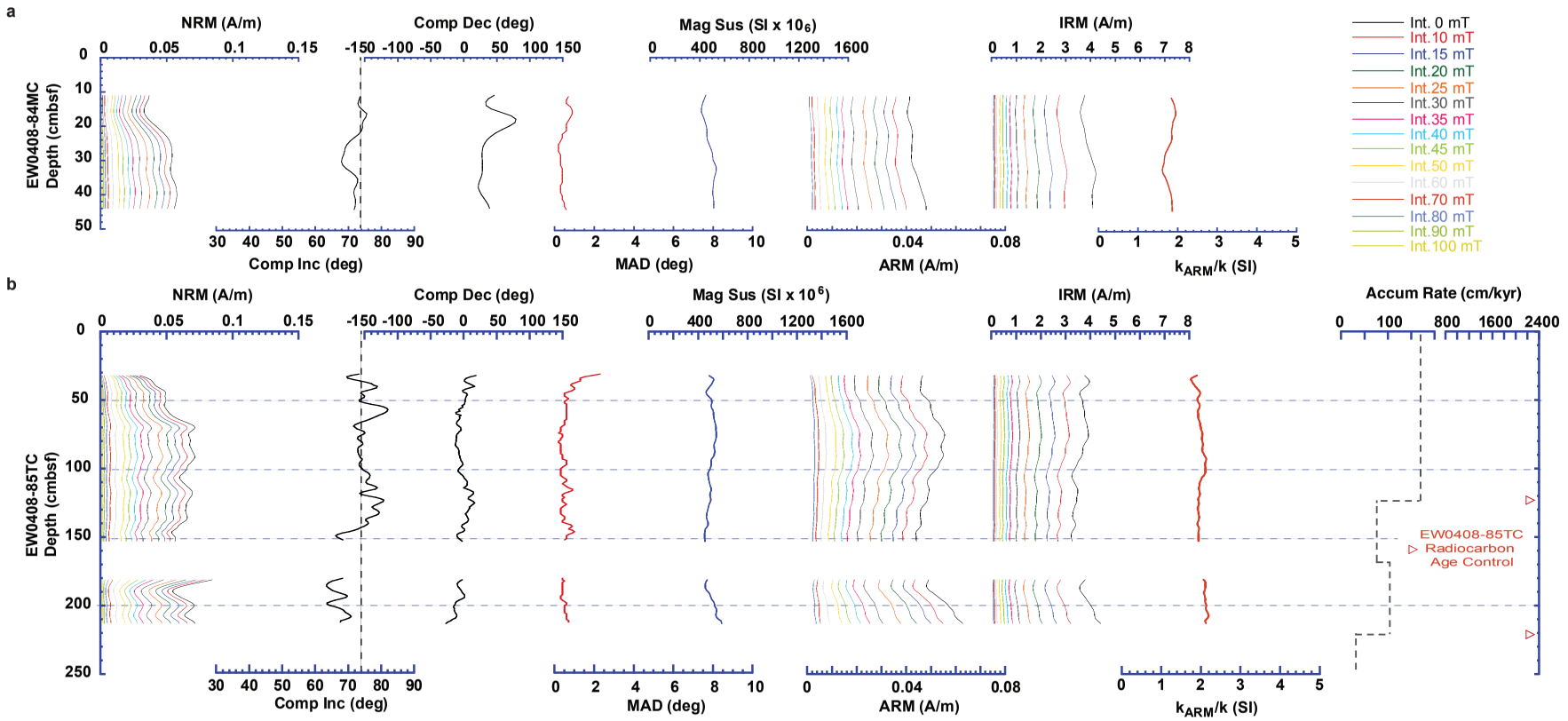
a
NRM (A/m)
Comp Dec (deg)
Mag Sus (SI x 10$_6$)
IRM (A/m)
EW0408-84MC
Depth (cmbsf)
Comp Inc (deg)
MAD (deg)
ARM (A/m)
k_{ARM}/k (SI)
Int. 0 mT
Int.10 mT
Int.15 mT
Int.20 mT
Int.25 mT
Int.30 mT
Int.35 mT
Int.40 mT
Int.45 mT
Int.50 mT
Int.60 mT
Int.70 mT
Int.80 mT
Int.90 mT
Int.100 mT
b
NRM (A/m)
Comp Dec (deg)
Mag Sus (SI x 10^6)
IRM (A/m)
Accum Rate (cm/kyr)
EW0408-85TC
Depth (cmbsf)
Comp Inc (deg)
MAD (deg)
ARM (A/m)
k_{ARM}/k (SI)
EW0408-85TC
Radiocarbon
Age Control

Figure A.3

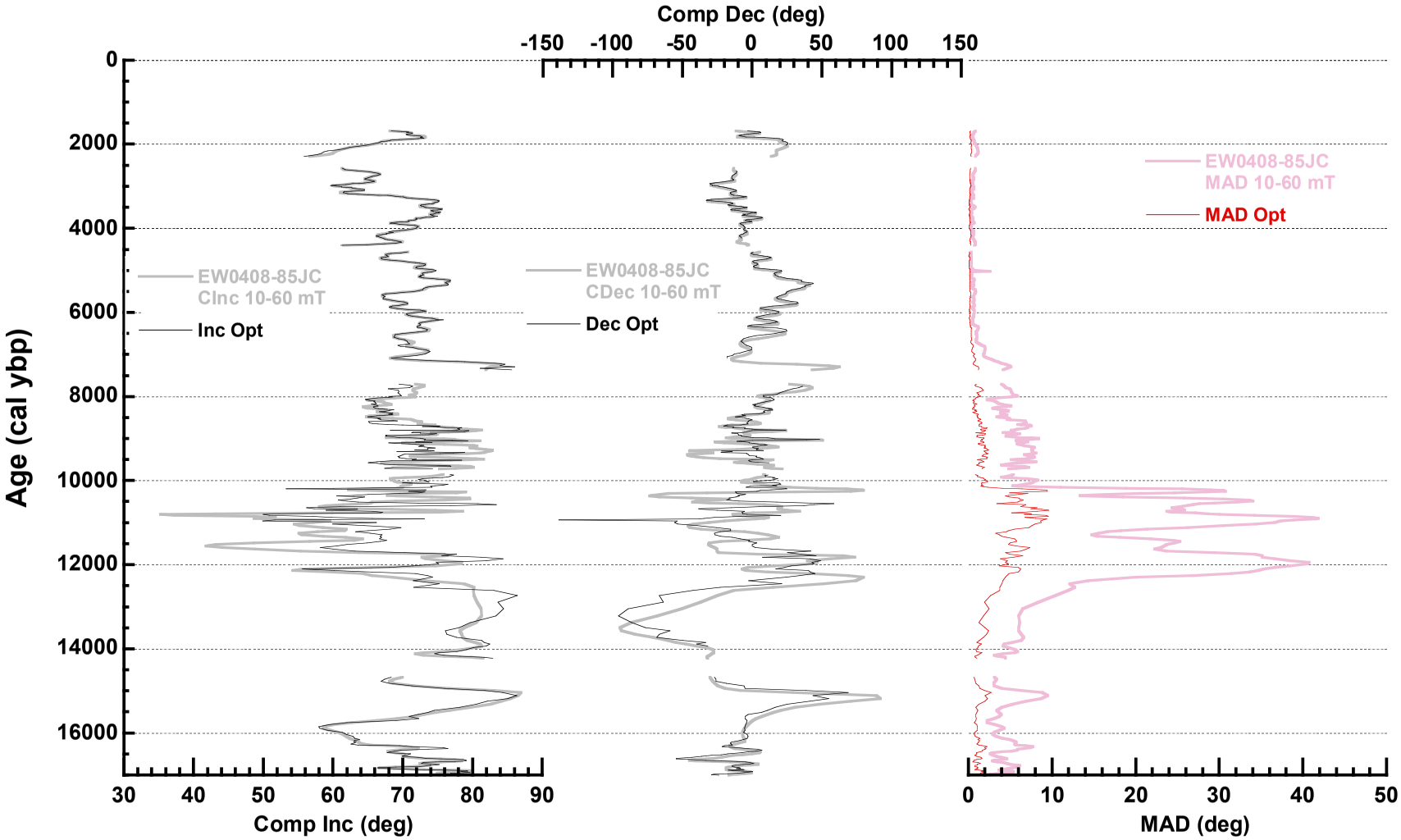
Comp Dec (deg)
-150
-100
-50
0
50
100
150
0
2000
4000
6000
8000
10000
12000
14000
16000
Age (cal ybp)
EW0408-85JC
CInc 10-60 mT
Inc Opt
EW0408-85JC
CDec 10-60 mT
Dec Opt
EW0408-85JC
MAD 10-60 mT
MAD Opt
30
40
50
60
70
80
90
Comp Inc (deg)
0
10
20
30
40
50
MAD (deg)

Figure A.4

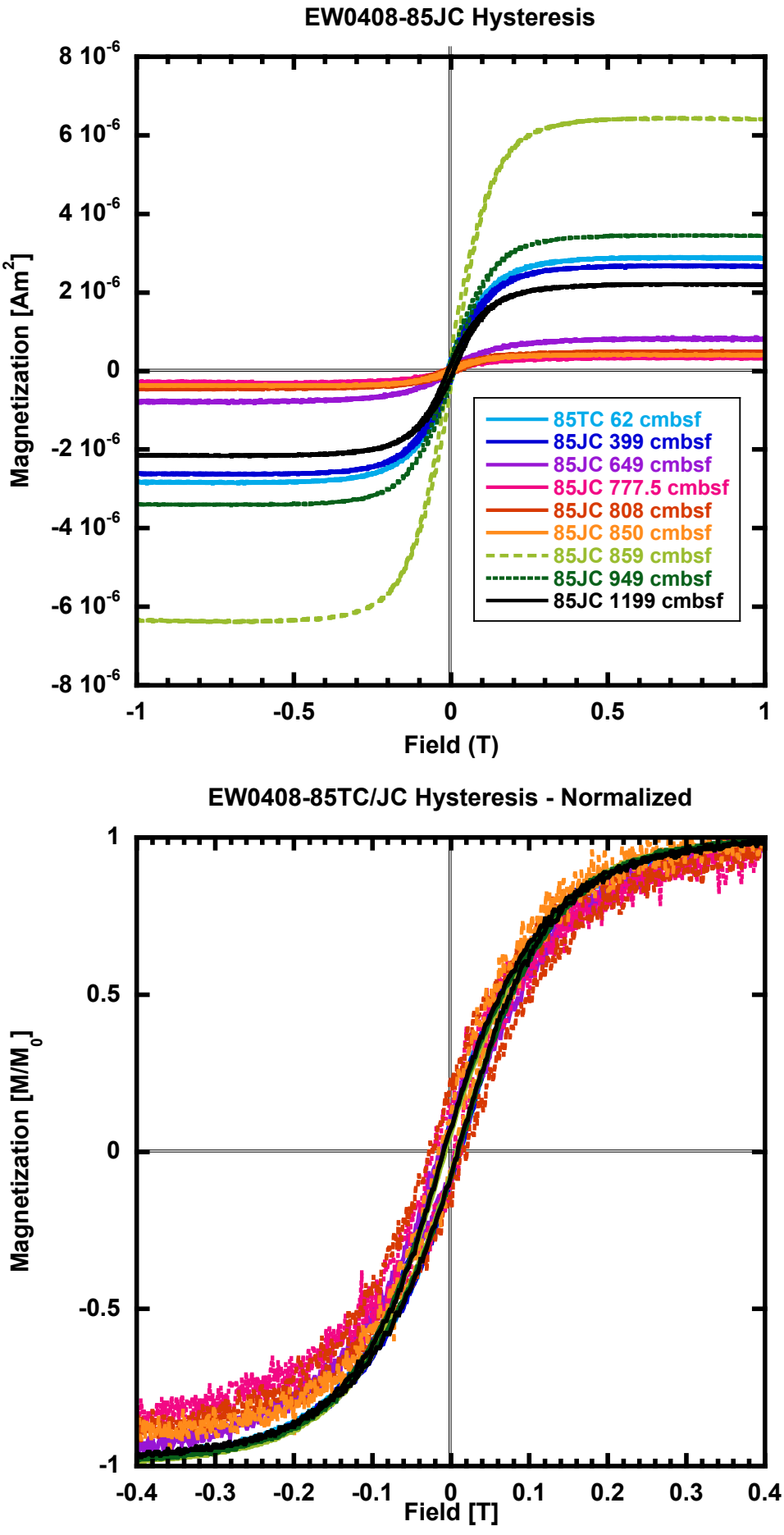
EW0408-85JC Hysteresis
Magnetization [Am^2]
8 10^{-6}
6 10^{-6}
4 10^{-6}
2 10^{-6}
0
-2 10^{-6}
-4 10^{-6}
-6 10^{-6}
-8 10^{-6}
-1
-0.5
0
0.5
1
Field (T)
85TC 62 cmbsf
85JC 399 cmbsf
85JC 649 cmbsf
85JC 777.5 cmbsf
85JC 808 cmbsf
85JC 850 cmbsf
85JC 859 cmbsf
85JC 949 cmbsf
85JC 1199 cmbsf
EW0408-85TC/JC Hysteresis - Normalized
Magnetization [M/M$_0$]
1
0.5
0
-0.5
-1
-0.4
-0.3
-0.2
-0.1
0
0.1
0.2
0.3
0.4
Field [T]

Figure A.5

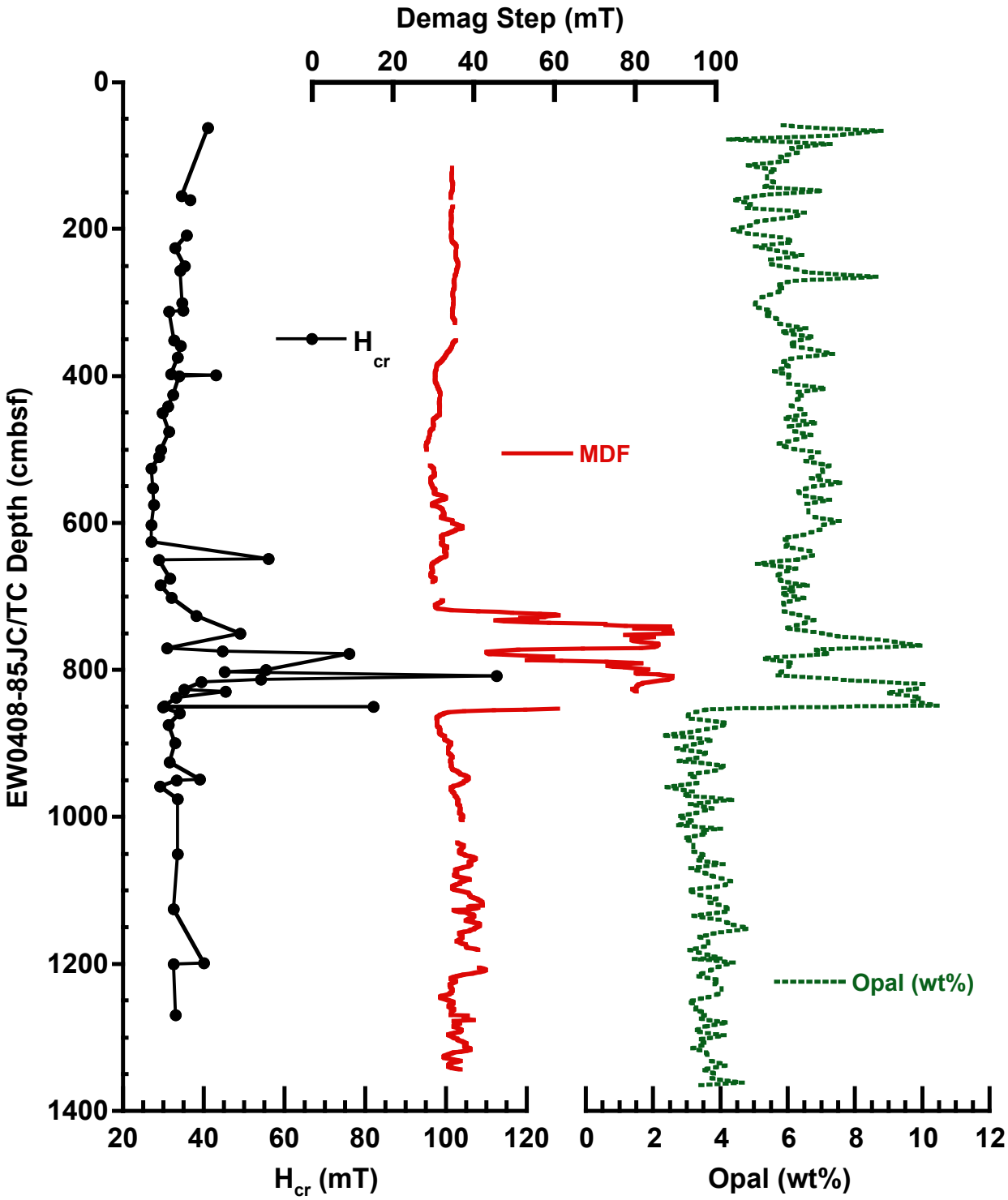
Demag Step (mT)
0
20
40
60
80
100
EW0408-85JC/TC Depth (cmbsf)
0
200
400
600
800
1000
1200
1400
H cr
MDF
Opal (wt%)
20
40
60
80
100
120
H cr (mT)
0
2
4
6
8
10
12
Opal (wt%)

Figure A.6

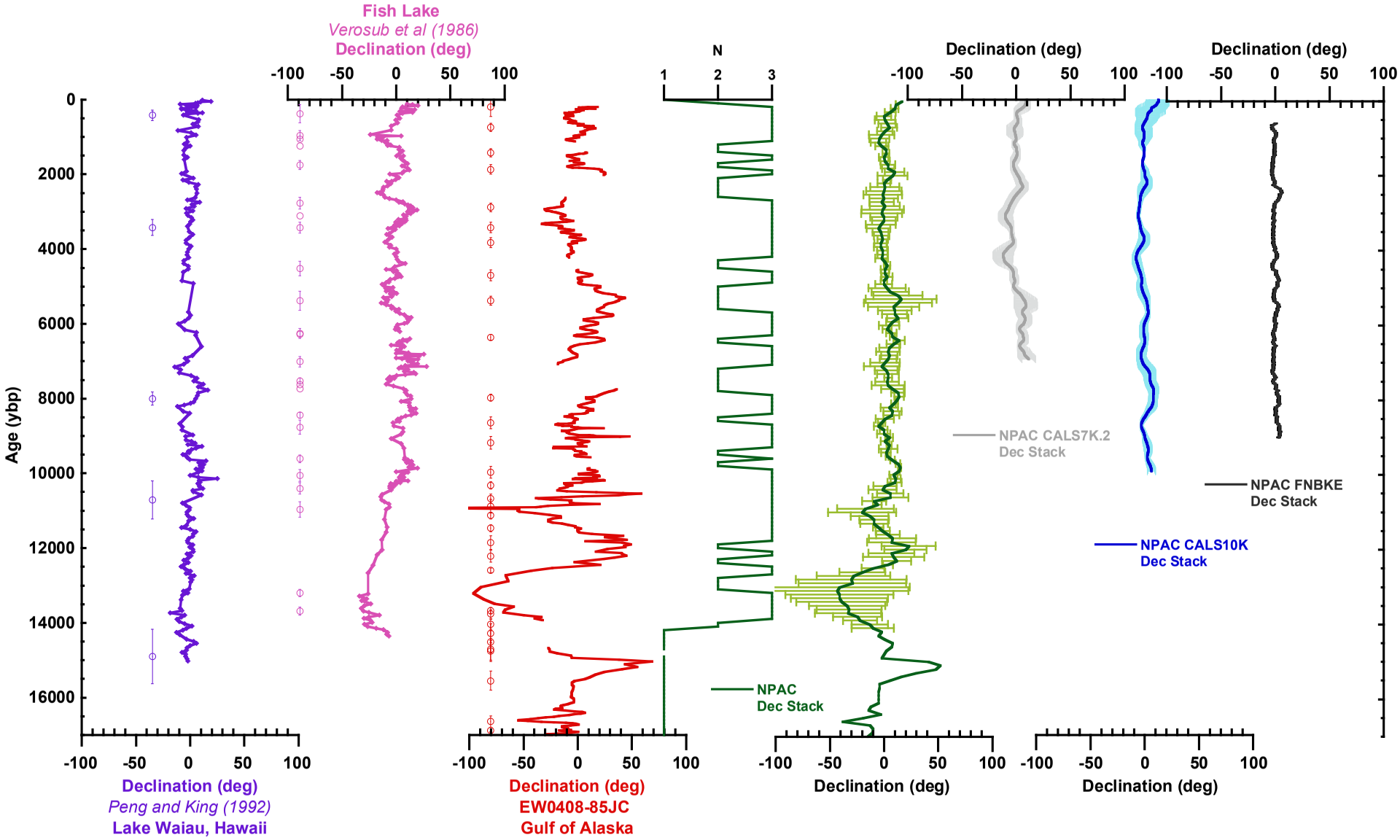
Fish Lake
Verosub et al (1986)
Declination (deg)
-100 -50 0 50 100
N
1 2 3
Declination (deg)
Declination (deg)
Age (ybp)
0
2000
4000
6000
8000
10000
12000
14000
16000
NPAC
Dec Stack
NPAC CALS7K.2
Dec Stack
NPAC FNBKE
Dec Stack
NPAC CALS10K
Dec Stack
Declination (deg)
Peng and King (1992)
Lake Waiau, Hawaii
Declination (deg)
EW0408-85JC
Gulf of Alaska
Declination (deg)
Declination (deg)

Figure A.7